Revealing 3D intragranular micromechanical fields at triple junctions

Sven E Gustafson, Wolfgang Ludwig, Raquel Rodriguez-Lamas, Can Yildirim, Katherine S Shanks, Carsten Detlefs, Michael D Sangid

Journal: Acta Materialia

Title: Revealing 3D intragranular micromechanical fields at triple junctions

Authors: Sven E. Gustafson[1], Wolfgang Ludwig[2,3], Raquel Rodriguez-Lamas[3], Can Yildirim[3], Katherine S. Shanks[4], Carsten Detlefs[3], Michael D. Sangid[1]

[1]School of Aeronautics and Astronautics, Purdue University, 701 W. Stadium Ave, West Lafayette, IN 47906

[2]University Lyon I, MATEIS, UMR5510 CNRS, 25 av. J. Capelle, 69621 Villeurbanne, France

[3]European Synchrotron Radiation Facility, 71 Avenue des Martyrs, 38000 Grenoble, France.

[4]Cornell High Energy Synchrotron Source, Ithaca, NY, USA

Keywords: high energy X-ray diffraction, dislocation density, strain gradients, heterogeneity, intragranular misorientation

Abstract: In polycrystalline solids, triple junctions (intersections of three or more grains) are regions with complex morphological compatibility requirements and are known to be locations of stress concentrations and strain localization. In this work, the intragranular lattice curvatures and elastic strains at triple junctions are investigated via a novel zoom-in style combination of synchrotron X-ray techniques. It is found that the highest values of intragranular misorientation metrics lie closer to triple junctions compared to grain boundaries (between two grains), and that the triple junctions exhibited higher values of these metrics. A heterogenous distribution of intragranular misorientations, elastic strains, and dislocation density was observed along a single triple junction line, with the two triple junction line end points (quad points) exhibiting different micromechanical fields. Finally, the calculation of the dislocation density via the Nye dislocation tensor is revisited. Specifically, the impact of considering elastic strain gradients to be negligible when constructing the Nye tensor is evaluated in a lightly-deformed grain. Similar magnitudes of lattice curvature and elastic strain gradients are found for a component of the Nye tensor. By not including the contribution of the elastic strain gradient, the dislocation density was underestimated at a hotspot region by 27% of the maximum dislocation density value in the entire reconstruction. This work provides a unique 3D view of triple junctions and highlights their spatially heterogenous micromechanical response, while also indicating the importance of including elastic strain gradients when evaluating the dislocation density.

1. Introduction

Triple junctions, a sub-set of grain boundaries, play a critical role in the deformation of polycrystalline structural alloys. While standard grain boundaries connect two grains, triple junctions connect three or more grains to form a network surrounding each grain. Grain boundaries in general act as barriers to dislocation motion and can cause dislocation pile up, leading to stress concentration and potentially crack initiation [1]. With the additional geometric compatibility constraint of multiple grains intersecting at triple junctions, elastic and plastic anisotropy has the potential to create a further concentration of stress. Past works have explored triple junctions and their ability to act as stress/strain concentrators and demonstrated that triple junctions can be

regions of either high or low stress [2,3]. However, additional investigation is required as past works have often focused upon: triple junctions in tricrystals, where the effect of a single triple junction is isolated [3], 2D surface measurements where the out-of-plane constraint is lacking [4], or computation models which may not fully capture the magnitude of localization at triple junctions [5,6]. 3D characterizations, with intragranular resolution, are needed to isolate triple junctions from grain boundaries and fully investigate the effect of triple junctions on the surrounding microstructure.

Past works have shown triple junctions behave differently during deformation than standard grain boundaries and that the stress state surrounding triple junctions is often multiaxial with steep gradients. Experimental microhardness testing examining triple junctions showed that hardening at triple junctions was lower at intersections of low-angle and special (coincident site lattice) boundaries as compared to randomly orientated grain boundaries [7]. Separating triple junctions from grain boundaries, nanohardness testing completed upon different spatial regions of a polycrystal demonstrated that triple junctions exhibited a harder response than general grain boundaries [8]. The studies, which found the stress response surrounding triple junctions to either increase or decay in the vicinity of triple junctions, indicated that the stress response is dependent on the elastic anisotropy between grains caused by orientation dependent stiffness differences [3] and the direction of loading with respect to the triple junction line [5]. However, experimental data capturing this complex microstructural response surrounding triple junctions is lacking, particularly from within the bulk of a polycrystal where influences from neighboring grains are present.

With the potential for stress concentration at triple junctions, past modeling studies have identified triple junctions as sites of crack initiation [9] and experimental fatigue testing further observed crack nucleation at triple junctions, particularly those composed of random grain boundaries [10]. Similarly, a recent 3D electron backscatter diffraction (3D-EBSD) investigation found that slip bands often formed at triple junctions made up of two or more random grain boundaries, highlighting the potential for additional slip activity near triple junctions [11]. Surface characterizations have also identified triple junctions as locations with stand-out local slip activity. Fine slip band structures were observed after very high cycle fatigue, primarily at triple junctions [12], and triple junctions have been observed to be local sites of multiple slip activation [13]. Additionally, a study in columnar-grained nickel found that for all triple junctions investigated, at least one grain displayed slip activation on a slip system, which deviated from the expected single crystal response [4]. In general, triple junctions have been found to be locations deviating from the bulk of the grain both in slip activity and as regions of highly multiaxial stress states highlighting the need for 3D experiments to capture intragranular metrics of both stress and plastic strain.

Such 3D characterization of the intragranular micromechanical fields would also allow for the investigation of the spatial gradients, and by extension, the dislocation density, further capturing the microstructural response near triple junctions. As introduced by Nye [14], the dislocation density can be related to the Nye dislocation tensor, which Kröner further related to the elastic distortion on the crystal lattice and thus spatial gradients in both lattice curvature and elastic strain

[15]. In recent years, advancements in experimental techniques have led to the introduction of high-resolution EBSD (HR-EBSD) where cross-correlation techniques allow for high angular and strain resolution surface measurements [16,17]. Through such techniques, or the 3D synchrotron X-ray technique differential aperture X-ray microscopy (DAXM), measurements of the local lattice distortion have been used to determine the dislocation density across multiple material systems [18–23]. Often, the contribution of elastic strain gradients in calculating the dislocation density is considered to be negligible compared to the gradients in lattice curvature; this is supported by measurements made in past works [19,23]. However, these measurements have either been made via 2D surface techniques, where out-of-plane measurements cannot be captured and stresses may relax, or relatively small volumes with few grains.

In this work, a full-field analysis of a bulk polycrystal is examined after cyclic loading to identify individual grains of interest for further high-resolution characterization of the intragranular plastic and elastic metrics via an innovative zoom-in approach. An Al-Li specimen was initially characterized with high energy X-ray diffraction microscopy (HEDM) and diffraction contrast tomography (DCT) to capture the entire volumetric microstructure, then individual grains were further examined via a zoomed-in technique using dark field X-ray microscopy (DFXM) for 3D interrogation of the micromechanical fields with high spatial and angular resolution. Statistical comparisons between triple junctions and grain boundaries are made to determine if the microstructure surrounding triple junctions presents a different micromechanical response than grain boundaries. Then the spatial heterogeneity along a single triple junction, extending from one quad point to another, is explored to demonstrate the heterogenous microstructural response possible along individual triple junctions. Finally, the relative contributions of elastic strain and lattice curvature gradients to the Nye dislocation tensor are compared to evaluate the negligibility of elastic strains in determining the dislocation density. Such investigations are made possible by linking multiple experiments across length scales to capture both the grain average and intragranular material response.

2. Material and Sample Preparation

Careful specimen and material development were needed to satisfy the experimental requirements of cyclic loading, HEDM, and DFXM. The specimen was designed to fit within the rotational and axial motion system (RAMS), which allows both cyclic loading and a full $360°$ unobstructed HEDM scan range [24]. To allow the timely interrogation of multiple grains via DFXM, cyclic loading was designed to impart only small amounts of plasticity to the specimen and prevent lengthy DFXM scan times due to the increased misorientation introduced during deformation. Lastly, DFXM required the specimen to: (i) be adaptable to fit upon the goniometer stage [25], (ii) have low attenuation to facilitate the desired X-ray energy without needing extraction methods as used in past works [26], and (iii) contain equiaxed structured grains with diameters less than $100\ \mu m$ to fit within the detector's field of view.

With these requirements, an Al-Li (2.5 wt% Li) binary alloy, with a TiB_2 grain refiner, was tailored specifically to meet the required material properties and specimen designed to facilitate easy HEDM and DFXM scanning. The material was cast, then hot rolled to a $6\ mm$ thickness, and finally cold rolled to a final thickness of $3.5\ mm$ with cold rolling direction perpendicular to the

hot rolling direction. With the plastic deformation induced from cold rolling to facilitate recrystallization, heat treatment trials were conducted to achieve the desired grain size and structure. These trials resulted in a final heat treatment of 3.5 minutes at $500°C$ followed by a water quench. An EBSD image of the resulting microstructure is shown in Fig. 1a with the majority of grain sizes measuring less than $100\ \mu m$ in diameter. During later HEDM scanning it was found that regions of the microstructure were left partially un-recrystallized; however, due to experimental capabilities, these regions were avoided during DFXM scanning and did not affect the scientific objectives of this work. Initial mechanical testing was completed upon dog-bone shaped specimens (Fig. 1c) which were machined via wire electrical discharge machining (EDM) with the loading axis along the hot rolling direction. Mechanical testing was done on a Mark-10 load frame, and the resulting stress versus strain plot is shown in Fig. 1b with the proportional limit determined to be $100\ MPa$. The final specimen design is shown in Fig. 2d with grips compatible for the RAMS device and a $500\ \mu m$ square cross section. These specimens were also machined via EDM with loading axis along the original hot rolling direction. Between the small cross section and choice of material, the specimen did not require further area reduction nor grain extraction to allow for DFXM characterization. After the HEDM experiment, the grips of the specimen shown in Fig. 2d were removed via EDM and the specimen was glued upon a cylindrical pin to fit in the DFXM goniometer stage; no cutting was conducted near the gauge section, maintaining the deformation state after cyclic loading.

3. High Energy X-ray Characterizations, Reconstructions, and Analyses

3.1. HEDM and DCT

HEDM characterization and cyclic loading was carried out at the Cornell High Energy Synchrotron Source (CHESS) followed by a secondary DCT characterization at the European Synchrotron Radiation Facility (ESRF). HEDM is a X-ray diffraction technique, which rotates a polycrystalline specimen (about the loading axis in this case) while exposed to high energy X-rays, collects the diffraction events upon downstream detectors, and reconstructs the diffracted signal to provide grain averaged information on each grain within the polycrystal [27]. Far-field HEDM (FF-HEDM) and near-field HEDM (NF-HEDM) were conducted at CHESS to provide: (i) the grain averaged orientations, elastic strain tensor, and centroid position (via FF-HEDM [28]) and (ii) the entire 3D polycrystalline microstructure (via NF-HEDM [29]). DCT [30], which provides similar morphological information as NF-HEDM, was later performed on the specimen at ESRF to facilitate registration and identification of individual grains of interest in the DXFM experiment. Further information on all techniques can be found elsewhere [27–30]. The HEDM experiments at CHESS, specifically at the Forming and Shaping Technology beamline (FAST), were conducted with a $41.991\ keV$ X-ray energy and FF-HEDM and NF-HEDM detector distances of $654\ mm$ and $6.44\ mm$, respectively. NF-HEDM used a detector system composed of a LuAg:Ce scintillator, $5x$ objective lens, and Retiga 4000DC CCD camera, which resulted in images with $2048\ x\ 2048$ pixels and a $1.48\ \mu m$ effective pixel size. FF-HEDM was conducted using two Dexela 2923 detectors producing images of $3888\ x\ 3072$ pixels of size $74.8\ \mu m$. All scanning was done via five diffraction volumes, each $220\ \mu m$ tall with $10\ \mu m$ overlap on either side, which spanned the $1\ mm$ gauge length. After completion of the experiment, HEDM reconstructions were

completed via HEXRD [28] on the individual diffraction volumes then all data was compiled via in-house MATLAB and Dream3D [31] scripts. The NF-HEDM reconstruction was performed with a $2\ \mu m$ voxel size and is shown in Fig. 2a, where only voxels with confidence greater than 0.6 are displayed. The DCT performed at ESRF (beamline ID11) was conducted with three overlapping diffraction volumes and captured the same region as NF-HEDM as shown in Fig. 2b. Conducted at $43.6\ keV$, each DCT scan took $7{,}200$ projections over $360°$ with a detector setup ($10\ \mu m$ LSO:Tb scintillator, $10x$ objective lens and Andor Marana scmos camera) which produced and effective pixel size of $1.22\ \mu m$. The HEDM and DCT reference frames were linked by determining the coordinate transformation which minimized the misorientation between the two microstructures of multiple known grains simultaneously; spatial registration was performed in Paraview [32].

The reconstructed and aligned microstructures of both HEDM and DCT are compared in Fig. 2c with average grain diameters of $31.6\ \mu m$ and $16.8\ \mu m$, respectively, and an observed (001) residual texture. The difference in grain size distribution, as shown in Fig. 2c is due to experimental differences; NF-HEDM and DCT can produce similar results given identical experimental conditions [33]. Here, a different X-ray flux and exposure time allowed DCT to capture smaller grains missed by HEDM resulting in DCT capturing $\sim 19{,}000$ grains, while HEDM captured $\sim 3{,}000$ grains. All grains characterized by DFXM were indexed by both HEDM and DCT. During the experiment at CHESS, the sample underwent cyclic loading to impart light deformation to the grains. The specimen was cycled in displacement control between displacement points set during the first cycle corresponding to $65\ MPa$ and $\sim 3\ MPa$ and the maximum displacement set point was maintained throughout cyclic loading resulting in stress relaxation as quantified in Fig. 3. The loading parameters were selected to impart deformation, while restricting the excessive lattice distortion that would prevent the use of DXFM characterization. The spatial distribution of grain averaged stresses within the specimen during loading is presented in Fig. 3 where the individual grain morphologies reconstructed via NF-HEDM are colored with their corresponding grain averaged stress along the loading direction as calculated from FF-HEDM. The grain averaged stress tensors were calculated from the elastic strains reconstructed from FF-HEDM via the anisotropic form of Hooke's law with stiffness values of $[C_{11}, C_{12}, C_{44}] = [110, 58, 30]\ GPa$ [34].

3.2. DFXM

With initial characterization and cyclic loading complete, multiple grains within the specimen were identified as grains of interest and zoomed into to enable higher resolution characterization of the intragranular characterization of lattice curvature and elastic strain via DFXM [35–38]. DFXM aligns a single grain such that a set of lattice planes are in the diffraction condition, illuminates a thin slice of the material ($typically\ < 1\ \mu m$), and rotates the grain via small orthogonal tilts shown in Fig. 4 as ϕ_{X_1} and ϕ_{X_2}. By placing an objective lens in the diffracted signal, the X-rays are both filtered, such that only X-rays within the numerical aperture of the microscope are transmitted, and magnified to produce a spatially distributed image on an area detector placed downstream. By applying small tilts about the orthogonal directions, the spatial distribution of two components of lattice curvature are probed, since only regions of the illuminated crystal lattice

that satisfy Bragg's law will diffract and transmit signal to the detector. Further, by sweeping the tilt of the objective lens along 2θ, the spatial distribution of lattice spacing is determined from which a single component of the elastic strain can be calculated:

$$\varepsilon = -\frac{1}{2}\frac{\Delta 2\theta}{Tan\left(\frac{2\theta}{2}\right)} \quad (1)$$

where, ε is the component of elastic strain normal to the lattice planes of interest, 2θ is the angle satisfying Bragg's law for the crystallographic planes of interest, and $\Delta 2\theta$ is the objective tilt which measures small deviations from 2θ. The value of a scanned component, ϕ_{X_1}, ϕ_{X_2}, or 2θ, for each voxel is calculated by summing the intensities along the other scanned components such that an intensity profile, as a function of a single component, is produced. The value of the single component for a voxel corresponds to the intensity profile's center-of-mass. Measurements of ϕ_{X_3} are not taken due to the experimental configuration. Through this technique, the angular and elastic strain values can be determined for each voxel with resolutions on the order of $0.005°$ and $5\ x\ 10^{-5}$ respectively [38,39].

DFXM characterization was conducted at ESRF (beamline ID06-HXM) on six individual grains with an energy of 17 keV. A condenser, consisting of 58 1D Be lenses, each with a $100\ \mu m$ radius, was placed $\sim 720\ mm$ upstream from the specimen to condense the incoming X-ray beam into a horizontal line of FWHM $\sim 700\ nm$. The {111} family of planes was chosen for characterization in this experiment due to their relevance to crystallographic slip during deformation of FCC metals. As such, the microscope was placed at the nominal Bragg angle of $\sim 17.98°$. An X-ray objective comprising 88 2D parabolic Be lenses was positioned $261\ mm$ downstream from the sample during scanning. In this position, the objective lenses resulted in a magnification of 18.15. A far-field detector (scintillator, 10x Mitutoyo objective and PCO.edge sCMOS camera), with $2560\ x\ 2160$ pixels, was placed $5\ m$ from the sample and, with the experimental setup, had an effective pixel size of $124\ x\ 40\ nm$. To connect the reference frames between HEDM, DCT, and DFXM the loading axis of the specimen was aligned approximately along the X_2 axis. For diffraction, the (111) lattice planes must have their normal aligned in the X_3, X_1 plane. To achieve this for grains within a polycrystal, tilts up to $\sim 12°$ about the other two axes were required. There are two distinct scan types, which will be discussed in this work, mosaicity scans and combined mosaicity and elastic strain scans. Mosaicity scans sweep through both ϕ_{X_1} and ϕ_{X_2} to capture the intragranular lattice curvature of the planes of interest. Combined mosaicity and elastic strain scans conduct multiple mosaicity scans along a range of 2θ values to additionally capture the intragranular elastic strain. Here, the mosaicity scans were all taken with a $[\phi_{X_1}, \phi_{X_2}]$ step size of $[0.04°, 0.01°]$ and range of at least $0.4°$ for each tilt (some scans required a larger tilt range to fully characterize the internal orientation spread). Combined mosaicity and elastic strain scans were conducted on one of the interrogated grains with the addition of a 2θ step size and range of $0.01°$ and $0.1°$, respectively. Due to the motion of the images upon the detector during scanning of 2θ caused by non-uniform vertical microscope movement, each set of images in a combined mosaicity and elastic strain scan were manually shifted in detector space prior to reconstruction [26]. Data reconstruction was completed via an in-house MATLAB script adapted from Simons et al. [35].

Individual DFXM scans are completed upon $\sim 700\ nm$ slices of a grain along X_3, and if multiple DFXM scans are taken for each grain, post experiment assembly is required to reconstruct the 3D morphology of each scanned grain. Each DFXM scan has its images cleaned by applying both a dark image subtraction and a universal intensity subtraction of 15 counts as determined by image inspection after dark subtraction. After cleaning, the multiple scans constructing each grain are stacked within MATLAB along the X_3 direction and a shift along X_1 is applied to each scan corresponding to the expected image movement upon the detector due to specimen translation. In some cases, a single grain was interrogated with multiple chunks of several scans, each during the experiment; the separate 3D spatial volumes resulting from such chunking of the grain were registered by matching morphological features of overlapping scans. Once the individual scans were stacked vertically, the 3D morphology of the grain was masked by removing all voxels with intensity less than 10% of the maximum and in the mosaicity reconstructions the grain boundary was smoothed via a 2D convolution applied to the individual slices (about X_1 and X_2). The threshold value was chosen to produce the most consistent morphological match between the grains in DCT and DFXM when superimposed in Paraview. To capture the expected higher deviations of ϕ_{X_1} and ϕ_{X_2} near the grain's boundary, mosaicity scans rocked the entire extent of each grain's ϕ_{X_1} and ϕ_{X_2} ranges. The 3D volumes produced via this method have a voxel size of $[X_1, X_2, X_3]$ size $[124,\ 40,\ \sim 600\ to\ 2{,}000\ ]\ nm$ where the final dimension is determined by the calculated translation of the specimen along X_3.

3.3. Intragranular Analysis Methods

Once each grain was reconstructed in 3D, metrics evaluating the intragranular misorientation, elastic strain, non-local curvature, and location of triple junctions were constructed. For each grain, the average values of ϕ_{X_1}, ϕ_{X_2}, and, where applicable, 2θ were calculated and subtracted from the 3D spatial arrays producing deviations in lattice curvature and elastic strain relative to the grain average. From these values, additional intragranular arrays were calculated. An intragranular misorientation (IGM) was calculated via the sum of squares of ϕ_{X_1} and ϕ_{X_2} at each voxel which describes the relative amount of lattice curvature deviation from the grain's average value. A 3D kernel average misorientation (3DKAM), similar to EBSD's 2D KAM, was calculated at each voxel to provide indication of local orientation changes. Here, 3DKAM was calculated by determining the mean misorientation between a voxel of interest and all neighboring voxels within $\sim 3\ \mu m$ (specifically a kernel cube of $[X_1, X_2, X_3]$ size $[3100\ nm,\ 2920\ nm,\ 3\ scans\ of\ height \sim 600\ to\ 2{,}000\ nm]$). The intragranular elastic strain, as calculated through Eq. 1, represents a relative elastic strain difference compared to the grain average. With the 3D morphology of each grain, a metric of curvature was constructed to indicate the degree of protrusion from or intrusion into the bulk of the grain; details of its calculation can be found in Appendix A. Finally, with spatial registration of the DFXM reconstruction into the DCT frame, the locations of all triple junctions were mapped onto each grain's surface. This was completed by first removing the grain of interest from the DCT reconstruction and dilating the surrounding grains to fill the void, then, in Paraview, the DCT grain IDs were mapped to each surface voxel of the DFXM reconstruction. Triple junctions were defined as any voxel within $1\ \mu m$ of the boundary between two adjacent grains upon the surface of the DFXM reconstructed grain.

Finally, with 3D intragranular orientation and elastic strain fields, lattice curvature, and elastic strain gradients were calculated to construct components of the Nye dislocation tensor [18,40]. The Nye tensor, α_{ij}, is related to the elastic distortion tensor, β_{ij}, via Eq. 2:

$$\alpha_{ik} = -\epsilon_{klj} \frac{\partial \beta_{ij}}{\partial x_l} \tag{2}$$

where ϵ_{klj} is the Levi-Civita (permutation) symbol. The elastic distortion on the lattice (Eq. 3) can be separated into the symmetric elastic strain tensor, ε_{ij}, (Eq. 4), and anti-symmetric lattice rotation tensor, ω_{ij}, (Eq. 5):

$$\beta_{ij} = \varepsilon_{ij} + \omega_{ij} \tag{3}$$

$$\varepsilon_{ij} = \begin{bmatrix} \varepsilon_{X_1X_1} & \gamma_{X_1X_2} & \gamma_{X_1X_3} \\ \gamma_{X_1X_2} & \varepsilon_{X_2X_2} & \gamma_{X_2X_3} \\ \gamma_{X_1X_3} & \gamma_{X_2X_3} & \varepsilon_{X_3X_3} \end{bmatrix} \tag{4}$$

$$\omega_{ij} = \begin{bmatrix} 0 & -R_{X_3} & R_{X_2} \\ R_{X_3} & 0 & -R_{X_1} \\ -R_{X_2} & R_{X_1} & 0 \end{bmatrix} \tag{5}$$

where R_{X_i} are counter-clockwise rotations about the principal directions and all indices are expressed in the DFXM lab frame. The (ϕ_{X_1}, ϕ_{X_2}) information collected during DFXM scans measures small changes to the lattice normal (lattice curvature), while the components of the elastic distortion tensor are measured to a first order approximation [41]. When only scanning a single set of lattice planes, DFXM measures the lattice curvatures ϕ_{X_1}, ϕ_{X_2}, and the component of elastic strain normal to the (111) planes of interest. As outlined in Appendix B, three components of β_{ij} were thus measured as:

$$\beta_{31} = \gamma_{X_1X_3} - R_{X_2} = -\phi_{X_2} \tag{6}$$

$$\beta_{32} = \gamma_{X_2X_3} + R_{X_1} = \phi_{X_1} \tag{7}$$

$$\beta_{33} = \varepsilon_{X_3X_3} = \varepsilon \tag{8}$$

With the geometry as described by Fig. 4, the measured elastic strain component is approximately along the X_3 direction (rotation about X_2 of half the Bragg angle $\frac{2\theta}{2} \approx 9°$). Without additional strain components, the measured component of elastic strain normal to the (111) planes of interest will be substituted here for $\varepsilon_{X_3X_3}$ and will be labeled simply ε. From the three measured components of the elastic distortion tensor, three components of the Nye tensor are calculated as:

$$\alpha_{31} = \frac{\partial \beta_{32}}{\partial_{X_3}} - \frac{\partial \beta_{33}}{\partial_{X_2}} = \frac{\partial \phi_{X_1}}{\partial X_3} - \frac{\partial \varepsilon}{\partial X_2} \tag{7}$$

$$\alpha_{32} = \frac{\partial \beta_{33}}{\partial_{X_1}} - \frac{\partial \beta_{31}}{\partial_{X_3}} = \frac{\partial \varepsilon}{\partial X_1} + \frac{\partial \phi_{X_2}}{\partial X_3} \tag{8}$$

$$\alpha_{33} = \frac{\partial \beta_{31}}{\partial X_2} - \frac{\partial \beta_{32}}{\partial X_1} = -\frac{\partial \phi_{X_2}}{\partial X_2} - \frac{\partial \phi_{X_1}}{\partial X_1} \quad (9)$$

With three individual components of the Nye dislocation tensor, the dislocation density can be estimated through an entrywise 1-norm [42] where a scaling of k is applied as appropriate for the number of components constructing the Nye tensor, which are collected from DFXM [21]:

$$\rho \approx k\frac{1}{b}\|\alpha\|_1 = k\frac{1}{b}\sum_i \sum_j |\alpha_{ij}| \quad (10)$$

Here, ρ is an estimation of the dislocation density and b is the magnitude of the Burgers vector as described by Eq. 11 for FCC crystals:

$$b = \frac{a}{\sqrt{2}} \quad (11)$$

where a is the unstrained lattice spacing as determined from HEDM for this specimen ($0.404532\ nm$). The scalar k has a value of $\frac{30}{9}$ when calculating the dislocation density including the contribution of the elastic strain gradients and $\frac{30}{7}$ when not including them [21]. Such an approximation of the dislocation density has been shown to reveal similar qualitative distributions as seen from methods which solve for separate dislocation types through minimization schemes [23]. Lastly, DFXM's ability to capture the spatial gradients in a sample with light deformation was evaluated by estimating the background noise observed in the reconstructions. The method described by Kamaya [43] for calculating the background noise in EBSD spatial gradients was adapted to estimate the background noise in the DFXM spatial gradients along each principal direction (X_1, X_2, X_3) and measured component ($\phi_{X_1}, \phi_{X_2}, \varepsilon$); details can be found in Appendix C. To increase the signal to noise ratio, the raw intensity data in the combined mosaicity and elastic strain dataset of a single grain was spatially binned prior to calculating the center-of-mass values for each measured component ($\phi_{X_1}, \phi_{X_2}, \varepsilon$) resulting in a voxel size, and therefore gradient step size of $[X_1, X_2, X_3] = [248,\ 240,\ 995]\ nm$. The background noise in the spatial gradients for the combined mosaicity and elastic strain scans was determined to be no more than $40\frac{1}{m}$ for the binned reconstruction.

4. Results

Six grains were interrogated through DFXM mosaicity scans and were then spatially linked to the overall DCT reconstruction (Fig. 5). From this spatial link, grains 2 and 3 were identified to share a coherent twin boundary, and the orientation relationship between these grains allowed simultaneous DFXM interrogation of their shared (111) planes. The DFXM reconstruction of these grains was later separated manually in Paraview by using the lower intensity observed along the coherent twin boundary as a guide. From Table 1, Grains 1-3 display much higher average values of IGM ($> 0.060°$) and 3DKAM ($> 0.015°$) as compared to grains 4-6 (IGM$< 0.025°$ and 3DKAM$< 0.008°$). The low average values of IGM and 3DKAM, and small size, of grains 4-6 are consistent with expectations of fully recrystallized grains [37]. As such, Fig. 6 displays all grains and Fig. 7 isolates grains 4-6 with adjusted IGM and 3DKAM color bars to better visualize their intragranular metrics. An excellent morphological match was observed between DCT and

DFXM (Fig. 6), and Table 1 presents the calculated volumes of each grain from both techniques. From the conducted range of the DFXM characterization, the entire morphologies of grains 3, 4, and 6 were captured based on comparison with the DCT reconstruction. Of these grains, two were within a 15% difference between the techniques, with DCT underestimating the grain volume. This underestimation is larger in grain 6, where its small size likely led to a relatively lower intensity in its indexed diffraction spots, thus producing a smaller reconstructed morphology.

The spatial distributions of the non-local curvature of grains 3, 4, and 6 were compared to each grain's triple junction network, IGM, and 3DKAM. Fig. 7 displays a zoomed in image of grain 4's non-local curvature to highlight the metric's ability to capture both protrusions from and intrusions into the bulk of the grain. Visual inspection of Figs. 6 and 7 found that triple junctions tended to run along regions of high non-local curvature, and that quad points often lay at local maxima of non-local curvature. A complex geometrical feature (cusp like) on grain 4 is identified by a red arrow in Fig. 7 and highlights 3D spatial complexities at grain boundaries that are not discernable with lower resolution/2D techniques. Notably, the DFXM mosaicity reconstruction measured grain 4's highest values of IGM and 3DKAM to be localized at this cusp with 0.20° and 0.08°, respectively. To investigate the possible connection between high values of IGM or 3DKAM (values in the 95th percentile) and non-local curvature, the voxels in the respective 95th percentiles of the IGM and 3DKAM were isolated from the rest of the grain's voxels, as shown in Fig. 6 and Fig. 7. From Fig. 8 it was found that for all three grains, the surface voxels in the 95th percentiles of both IGM and 3DKAM exhibited, on average, higher values of non-local curvature than arbitrary surface voxels. In general, this points to protrusions from the grain's surface tending to exhibit greater values of IGM/3DKAM than intrusions into the grain's surface.

The intragranular microstructural behavior at triple junctions was statistically and visually compared to that of grain boundaries for grains 3, 4, and 6. To do this, grain boundaries were defined as all voxels within 1 μm of each grain's surface, and triple junctions as all voxels within 1 μm of the networks shown in Figs. 6 and 7. All statistical comparisons were made via two-sample T-tests (t(degrees of freedom) = t statistic) with a significance level of 0.01. It was first investigated if high values of IGM and 3DKAM tended to lie spatially closer to triple junctions than grain boundaries. From Fig. 9 and Table 2, it was found that for all grains, the voxels in the 95th percentile of IGM tended to lie closer to triple junctions than grain boundaries; grains 4 and 6 showed a similar trend with 3DKAM. The reverse trend was then explored: if the measured values of IGM and 3DKAM at triple junctions were higher than at grain boundaries. From Fig. 10 and Table 3, triple junctions of all grains displayed statistically higher values of IGM and 3DKAM than grain boundaries. The triple junctions of grains 4 and 6 exhibited larger values of 3DKAM. For all grains, the local microstructure at triple junctions exhibited both larger deviations of lattice curvature from the grain average (IGM) and often greater local misorientation (3DKAM) compared with similar values measured at grain boundaries.

Spatial gradients of lattice curvature and elastic strain were calculated from a combined mosaicity and elastic strain reconstruction of grain 4, and then compared to investigate each gradient's relative contribution to the Nye tensor. Fig. 11 provides the spatial link between the mosaicity reconstruction of grain 4 and the combined mosaicity and elastic strain reconstruction. The red arrow in Fig. 11 is spatially consistent to that in Fig. 7, and the reference frames $[\mathcal{X}, \mathcal{Y}, \mathcal{Z}]$ and $[X_1, X_2, X_3]$ were equivalent during DFXM scans of grain 4. Fig. 12 displays the gradients of lattice curvature and elastic strain from perspective 2 (Fig. 11), with the black arrow identifying a hotspot region spatially close to the cusp of Fig. 7 ($\sim 2\ \mu m$). The magnitudes of these gradients, particularly at grain boundaries and the identified hotspot, were greater than the expected background noise of $40 \frac{1}{m}$, often by an order of magnitude. Three components of the Nye tensor were calculated from Eqs. 7-9 and displayed in Fig. 13, with cumulative distribution plots comparing the relative contributions from each spatial gradient term. Statistical comparisons were also made between the two spatial gradients contributing to each Nye tensor component. Notably, the average magnitude of the gradient of elastic strain contributing α_{31} was statistically greater than that of the lattice curvature ($t(453852) = 29.1, p < 0.01$). Comparisons of the other two Nye tensor components indicated that the gradients of ϕ_y were larger than, although still comparable to, the gradients of either ϕ_x or the elastic strain. Overall, the contributions to the Nye tensor were considered, with the elastic strain gradients displaying similar magnitudes to the gradients of lattice curvature.

The intragranular metrics, including the dislocation density, are extracted to highlight the measured spatial heterogeneity along an individual triple junction. Fig. 14 displays the intragranular metrics surrounding an outlined triple junction of grain 4 from perspective 1 (Fig. 11). Here the dislocation density was calculated from the measured components of the Nye tensor via Eq. 10 and all intragranular metrics were extracted in Paraview just subsurface ($\sim 1\ \mu m$) from the outline shown in Fig. 14b. Line plots of the extracted data, extending from quad point A to quad point C are shown in Fig. 15. Large spreads, relative to the grain averages, are seen in the intragranular metrics along the examined $25\ \mu m$ triple junction. In grain 4, the grain averages of IGM and 3DKAM from the mosaicity scan are $0.0244°$ and $0.0067°$, respectively. The variation of the IGM and 3DKAM, $0.037°$ and $0.025°$, respectively, from one point to another along the triple junction are greater than the grain average values of these metrics. Similar variability in the elastic strain is measured with a difference of $2.1\ x\ 10^{-4} \frac{mm}{mm}$ along the triple junction, compared to the average magnitude of only $1.11\ x\ 10^{-4} \frac{mm}{mm}$. In Fig. 15d, the spatial heterogeneity is of particular note where the dislocation density is measured to increase by $1.2\ x\ 10^{13} \frac{1}{m^2}$ from one end to another, a change of over $5x$ the average value ($2.1\ x\ 10^{12} \frac{1}{m^2}$). Exhibiting significant spatial heterogeneity, the intragranular metrics were all found to vary by more than the measured grain averages along a single $25\ \mu m$ triple junction.

5. Discussion

For multiple grains, statistical differences in the spatial distributions of both the IGM and 3DKAM identified triple junctions to exhibit greater values as compared to grain boundaries. General grain boundaries are regions where two deformation fields intersect and, to maintain compatibility, the differences in these fields must be accommodated by elastic strains (stresses), crystallographic slip (often additional slip system activation), or both [44,45]. By extension, the crystal lattice at triple junctions must similarly facilitate compatibility between three or more intersecting deformation fields. With an additional constraint imposed by a third grain, triple junctions have been identified in past works as regions of localized multiple slip activation [11,13] and increased dislocation density [20]. In this work, metrics of plastic strain are captured through IGM and 3DKAM. IGM measures the deviation in lattice curvature from the grain average and 3DKAM captures local misorientation similar to EBSD's KAM, which has been linked to dislocation density, specifically geometrically necessary dislocations (GNDs) [46,47]. Unlike 2D investigations, the 3D characterization here is capable of identifying all hotspots and localizations of extreme deviations in lattice curvature and high local misorientation that exist within a grain. With this in mind, it was found for multiple grains that the highest values, thus hotspots and localizations, of IGM and 3DKAM lay statistically closer to triple junctions than grain boundaries. Further, triple junctions, in general, exhibited greater values of IGM and 3DKAM than grain boundaries. These findings highlight that with the requirement to satisfy compatibility between three or more grains, the lattice near the triple junctions must misorient (deform), both locally and from the grain average, more than standard grain boundaries.

At a grain boundary in a polycrystal, the local deformation is known to be heterogenous as a consequence of maintaining compatibility between grains; however, without 3D non-destructive characterization, the micromechanical state at the boundary between deeply embedded grains cannot be measured accurately. Here, with 3D characterization of a grain within the bulk of a specimen, the local micromechanical state at the interface between grains is preserved and measured. Deformation at the interfaces between grains is influenced by the orientation and micromechanical state of the neighboring grains during loading. As a result of this interaction, Fig. 15 demonstrates the significant spatial heterogeneity characterized along a single triple junction in grain 4. Additionally, the result of many local grain interactions is captured and highlighted between the two quad points at either end of the triple junction. Specifically, quad point C exhibits far larger values of IGM and 3DKAM than quad point A, with quad point C acting as the local maxima of IGM and 3DKAM and quad point A the local minimum. Further, the dislocation density of quad point A ($2.5\ x\ 10^{12}\ \frac{1}{m^2}$) is only slightly elevated from the grain average ($2.1\ x\ 10^{12}\ \frac{1}{m^2}$), while at quad point C the dislocation density is $5x$ greater ($1.1\ x\ 10^{13}\ \frac{1}{m^2}$). As these dislocation densities were calculated from measurements of only one (111) reflection, they are likely underestimated; however, by interrogating a (111) plane, the plane on which slip occurs in FFC crystals, the majority of dislocations should be captured. By non-destructively interrogating the entire length of a triple junction in 3D, the consequence of local grain interactions during loading is preserved and vastly different microstructural responses are measured at the two quad points of the triple junction. Such a finding highlights the importance of characterizing the intact, post-deformation micromechanical state to ensure the degree of heterogeneity at grain boundaries is accurately measured.

The contribution to the Nye tensor from the elastic strain gradients were found to be comparable in magnitude to that of the lattice curvatures. This finding is contrary to many past works from HR-EBSD and DAXM [23,48]. Here, there are likely multiple influencing factors leading to similar magnitudes of the elastic strain and lattice curvature gradients. Specifically, the measurements in this work were taken within the bulk of the polycrystal, upon a deeply embedded grain, where elastic strains (thus stresses) are not relieved and the influence of all adjacent grains is maintained, which is not the case in surface measurements. Additionally, DFXM is capable of capturing hydrostatic strains unlike EBSD and DAXM (though this has been seen to have relatively little effect on dislocation density [22]). Finally, to contextualize this finding, grain 4 is a relatively small grain in a specimen which underwent only light deformation; further work would be needed to quantify the relative contributions for grains exhibiting higher dislocation densities. These findings demonstrate that the gradients in elastic strain are similar in magnitude to the lattice curvatures, and that care should be taken to evaluate the elastic strains prior to assuming their negligibility when constructing the Nye tensor.

Accurate measurements of the dislocation density are critical in identifying localized regions of deformation. To quantify the information lost when neglecting the elastic strain gradients in grain 4, Fig. 16 views the dislocation density through perspective 2 and indicates a line stretching between two hotspots. In Fig. 17, the intragranular information along this line is extracted and two cases of the dislocation density are shown, one where the elastic strain gradient is included in the calculation and the other where it is assumed to be negligible. Fig. 17a shows that the trends in the dislocation density are still captured if the elastic strain gradient is ignored. Although, in neglecting the elastic strain gradients, an accurate measurement of the magnitude of dislocation density is lost in critical regions such as the hotspots at points D and E. At points D and E, without accounting for elastic strain gradients, the dislocation density is overestimated by 37% and underestimated by 27%, respectively, relative to the maximum value seen in the entire reconstruction ($2.1\ x\ 10^{13}\ \frac{1}{m^2}$). With increasing plastic deformation, GND's will continue to localize (at features such as sub-grain boundaries and slip band-grain boundary intersections), and create additional hotspot regions where elastic strain gradients may be substantial. With localizations of high dislocation density (specifically GNDs) being an indicator of damage, characterizations exploring such phenomena must accurately capture the magnitude of dislocation density which, as shown here, requires the measurement of elastic strain gradients.

6. Conclusions

Triple junctions are spatial features within all polycrystals with complex geometric compatibility requirements due to the intersection of multiple crystallographic orientations. As such, triple junctions are known sites of stress/strain localization; however, a grain's triple junction network, in comparison to its grain boundaries, as well as the entire length of individual triple junctions, have yet to be thoroughly examined due to the sparseness of high-resolution 3D experimental datasets. Here, a 3D investigation has been completed by using multiple synchrotron X-ray techniques to enable targeted zoom-ins onto multiple grains to characterize the intragranular micromechanical fields along all triple junctions. This characterization allowed for voxels close

to triple junctions to be statistically compared to voxels close to grain boundaries. From the analysis of multiple grains in various states of deformation, several findings are presented:

- For multiple grains, the high values (95^{th} percentile) of IGM and 3DKAM were shown to be statistically closer to triple junctions than grain boundaries; both IGM and 3DKAM quantify the degree of lattice curvature at each point within a grain. Similarly, triple junctions exhibited statistically higher values of both IGM and 3DKAM as compared to grain boundaries. Such high values of IGM point to triple junctions, as regions known for localized slip activity differing from the rest of the grain, necessitating large deviations of the lattice from the grain average. Additionally, with 3DKAM indicating more local changes in the lattice, high values point to a higher presence of GNDs to facilitate compatibility at triple junctions. These findings clearly demonstrate that triple junctions not only act differently than the bulk of the grain, but separate themselves from grain boundaries, with increased lattice curvature and local misorientation.
- A heterogenous distribution of all investigated intragranular metrics is observed along a single triple junction, with metrics such as dislocation density varying by $5x$ the grain average. The two quad points at either end of the $25\ \mu m$ long triple junction exhibited demonstratively different responses, with one exhibiting the local minimum and the other the local maximum of both IGM and 3DKAM. With deformation at triple junctions influenced by its multiple adjacent grains, this finding emphasizes the need for 3D non-destructive characterizations to measure the local micromechanical state, and ensure the degree of heterogeneity is preserved at triple junctions.
- The elastic strain gradients exhibited similar contribution to the Nye tensor compared to the gradients in lattice curvature. Specifically, in the α_{31} component, where both the elastic strain and lattice curvature gradients demonstrated large magnitudes, the values of the elastic strain gradient were, on average, statistically larger than those of lattice curvature. In demonstrating the significant contributions of both elastic strains and lattice curvatures in constructing the Nye tensor, this finding for a grain exhibiting a relatively low dislocation density ($10^{13}\frac{1}{m^2}$) indicates the need for caution when neglecting the elastic strain in calculations of the intragranular dislocation density via the Nye tensor in structural alloys. This is highlighted by hotspot regions, where the removal of the elastic strain gradient contributions caused deviations in the dislocation density by 37% of the maximum density observed.

This work provided a previously unexplored 3D view of triple junctions to expose the spatial complexity of intragranular micromechanical fields surrounding triple junctions and points to the need to consider triple junctions, known sites of stress and strain localization, in 3D with the surrounding microstructure left intact, to fully capture the their heterogenous nature.

Declaration of Competing Interest

The authors declare that they have no known competing financial interests or personal relationships that could have appeared to influence the work reported in this paper.

Acknowledgements

This work was primarily supported by the National Science Foundation under grant number CMMI 16-51956, as well as Sandia National Laboratories under contract number 2189722 under the Laboratory Directed Research and Development program. This work is based on research conducted at the Center for High-Energy X-Ray Sciences (CHEXS), which is supported by the National Science Foundation (BIO, ENG, and MPS Directorates) under award DMR-1829070. The diffraction contrast tomography and dark field X-ray microscopy was performed at the European Synchrotron Radiation Facility where we acknowledge the provision of synchrotron radiation facilities. We would like to thank Dr. Markus Heinimann and Cagatay Yanar at Arconic for casting and hot rolling of the material and Professor David Johnson and Dr. B. Stiven Puentes at Purdue University for their assistance with cold rolling and material tailoring. Additionally, the authors thank both Dr. Peter Ko at CHESS and Mads Carlsen at ESRF for their assistance during beamtime.

Sandia National Laboratories is a multimission laboratory managed and operated by National Technology & Engineering Solutions of Sandia, LLC, a wholly owned subsidiary of Honeywell International Inc., for the U.S. Department of Energy's National Nuclear Security Administration under contract DE-NA0003525. This paper describes objective technical results and analysis. Any subjective views or opinions that might be expressed in the paper do not necessarily represent the views of the U.S. Department of Energy or the United States Government.

Appendix A: Non-Local Curvature

The goal of the non-local curvature calculated in this work is to provide a measure of the protrusion from or intrusion into the bulk of a grain in the region surrounding each surface voxel. With the high aspect ratio voxel size of DFXM, standard meshing or Delaunay methods proved insufficient to capture the grain's surface without losing spatial resolution. As such, a method to calculate a metric of protrusion/intrusion is described below and the result is shown in Fig. 6 and Fig. 7. A zoomed in image of the non-local curvature of grain 4 is shown in the lower right corner of Fig. 7.

The methodology is broken into two steps: initial calculation of curvature at each voxel then smoothing. At each voxel, three orthogonal slices of the grain's boundary are taken with respect the DFXM frame. A schematic illustrating the relevant geometry is shown in Fig. A1 where a hypothetical slice is taken orthogonal to $\mathcal{X}$ and $\mathcal{Y}$. Upon each orthogonal slice, a value of 'curvature' (defined here as κ) is determined for the voxel of interest. To do this, two lines are drawn to two other surface voxels on the orthogonal slice which are both $\sim 5\ \mu m$ away, one on either side of the voxel of interest. A third line is then drawn between these two voxels forming a triangle; the distance from the voxel of interest to the midpoint of this third line is defined as the 'curvature' for the orthogonal slice. The sign of the value is positive if the midpoint described lies inside the grain's surface, negative otherwise. For points not on the grain boundary in the $\mathcal{XY}$ plane, yet are on the boundary of other orthogonal slices, an $\mathcal{XY}$ κ value is estimated through a weighted summation of all κ values on the $\mathcal{XY}$ boundary. The weights are the squared distances between the voxel of interest and each voxel on the $\mathcal{XY}$ boundary; this method was found to produce reasonable estimations of κ. This procedure is completed for the remaining orthogonal slices, providing three values of κ at each surface voxel. A smoothing operation was then performed which took all curvature values in the surrounding $2\ \mu m$ region, and, using the surface

area of each individual voxel as weights, determined the weighted sum of these three 'curvature' values. The three values, one from each orthogonal slice, were then summed at each voxel to provide a total non-local curvature at each voxel which is displayed in this work.

Appendix B: X-ray Diffraction from a Weakly Distorted Lattice

The following is adapted from Ahl [41] into the coordinate system and notation defined in this work. As derived by Ahl to a first order approximation, the undistorted and distorted reciprocal lattice vectors are related by the elastic distortion tensor, β_{ij}:

$$\vec{g}' = (I - \beta^T)\,\vec{g} \tag{B1}$$

where $\vec{g}$ is the undistorted reciprocal lattice vector (along the lattice normal), $\vec{g}'$ the distorted reciprocal lattice vector, and I is the identity matrix. Given the DFXM lab frame of X_1, X_2, X_3, small deviations of the lattice normal are measured from $\vec{g}_0 = g_0\hat{X}_3$ through the counter-clockwise tilts of ϕ_1 and ϕ_2.

Small changes of the scattering angle 2θ are also measured by DFXM, and are related to axial strain via Eq. 1. Relating ε to the distorted reciprocal lattice vector and the grain average lattice spacing d_0:

$$g' = \frac{2\pi}{d_0(1+\varepsilon)} \tag{B2}$$

For small strains, and with $g_0 = \frac{2\pi}{d_0}$, the change in length of the reciprocal lattice vector is:

$$g' = (1 - \varepsilon)\,g_0 \tag{B3}$$

With this, Eq. B1 can be re-written to express the distorted reciprocal lattice vector in terms of the measurements made in DFXM:

$$\vec{g}' = (I - \beta^T)\,g_0\hat{X}_3 = \begin{bmatrix} g'_{X_1} \\ g'_{X_2} \\ g'_{X_3} \end{bmatrix} = g_0 \begin{bmatrix} \phi_2 \\ -\phi_1 \\ 1 - \varepsilon \end{bmatrix} \tag{B4}$$

From Eq. B5, three components of the elastic distortion tensor are thus measured:

$$\beta_{31} = \gamma_{X_1X_3} - R_{X_2} = -\phi_{X_2} \tag{B5}$$

$$\beta_{32} = \gamma_{X_2X_3} + R_{X_1} = \phi_{X_1} \tag{B6}$$

$$\beta_{33} = \varepsilon_{X_3X_3} = \varepsilon \tag{B8}$$

From the three components of β_{ij} identified here, the α_{3i} components of the Nye tensor are calculated as defined in Eqs. 7-9. Measurements of the other components of the Nye tensor require DFXM interrogation of additional, non-coplanar, lattice planes.

Appendix C: DFXM Spatial Gradient Noise Floor Determination

DFXM is capable of capturing orientation and elastic strain differences with sensitivity on the order of $0.005°$ and $5\ x\ 10^{-5}$, respectively [38,39]; however, a thorough investigation of the noise floor experienced in spatial gradients from the resulting 3D reconstructions has not been completed. Such an investigation is critical to ensure that the measurements, and any gradients calculated, are above the background noise observed. Particular to DFXM, each angular and elastic strain measurement $(\phi_{\mathcal{X}}, \phi_{\mathcal{Y}}, \varepsilon)$ is conducted with a different angular step size and the spatial resolution that is unique in all three principal directions $(\mathcal{X}, \mathcal{Y}, \mathcal{Z})$, requiring each measurement and direction to be probed to ensure all relevant measurements are above the corresponding noise floors. Here, the approach proposed by Kamaya [43] for determining the intragranular orientation background noise in EBSD scans is modified and applied to DFXM. With the noise floor between individual pixels determined, the minimum sensitivity in computed spatial gradients is found via Eq. C1 [49]:

$$\left(\frac{\partial M_i}{\partial X_j}\right)_{BG} = \frac{(\Delta M_i)_{BG_j}}{\Delta X_j} \tag{C1}$$

where M_i represents one of the angular/strain component measurements $(M_1, M_2, M_3) = (\phi_{\mathcal{X}}, \phi_{\mathcal{Y}}, \varepsilon)$, ΔX_j is the gradient step size along a principal direction in the DFXM frame $(X_1, X_2, X_3) = (\mathcal{X}, \mathcal{Y}, \mathcal{Z})$, and ΔM_i is the average difference in a single angular/strain component between a voxel and the voxels on either side along a principal direction. $(\Delta M_i)_{BG_j}$ is the determined background noise for a particular M_i and principal direction X_j. Lastly, $\left(\frac{\partial M_i}{\partial X_j}\right)_{BG}$ is the corresponding noise floor in the associated spatial gradient.

The ΔM_i calculation is performed multiple times at each voxel for single M_i and X_j, each time determining ΔM_i using voxels progressively further away from the voxel of interest along each principal direction. To assist in visualization of this calculation, the voxel layout is shown in Fig. C1 for a single principal direction, where ΔM_i is calculated between first voxel positions 0 and 1, then 0 and 2, and so on. As distance (voxel position) from the voxel of interest (voxel 0) increases, the calculated value of ΔM_i is expected to increase. Fig. C2 shows the resulting average ΔM_i for each angular/strain component along each direction as a function of distance for the combined mosaicity and elastic strain scans of grain 4 shown in Fig. 11. Here, two datasets are shown, un-binned data with voxel size $[124, 40, 995]\ nm$ and binned data with voxel size $[248, 240, 995]\ nm$. Voxel binning was introduced prior to the calculation of $(\phi_{\mathcal{X}}, \phi_{\mathcal{Y}}, \varepsilon)$ center-of-mass values to increase the signal to noise ratio in DFXM measurements by summing the intensity profiles from multiple pixels after initial image processing was completed. The binned dataset with voxel size of $[248, 240, 995]\ nm$ was used for all calculations of spatial gradients for the manuscript.

The observed background noise in the spatial gradients were then calculated and found to be below the values of gradients observed in Fig. 12. As outlined by Kamaya, the y-intercept of each plot in Fig. C2 represents the expected magnitude of background noise, $(\Delta M_i)_{BG_j}$; these values are tabulated for both un-binned and binned datasets in Table C1. The corresponding background noise in the spatial gradients, as calculated from Eq. C1 are tabulated; the binned data, as used in

the manuscript, displayed a general noise floor of $< 40\frac{1}{m}$. The spatial gradients shown in Fig. 12, particularly those indicated by the black arrow which are of interest in this work, are larger than the estimated minimum sensitivity of the DFXM scans, and further demonstrate DFXM's ability to resolve structural changes with high angular and spatial resolution.

References

[1] J.A. Ewing, J.C.W. Humfrey, The Fracture of Metals under Repeated Alternations of Stress, Philos. Trans. R. Soc. A Math. Phys. Eng. Sci. 200 (1903) 241–250. https://doi.org/10.1098/rsta.1903.0006.

[2] V. Tvergaard, J.W. Hutchinson, Microcracking in ceramics induced by thermal expansion or elastic anisotropy, J. Am. Ceram. Soc. 71 (1988) 157–166.

[3] C.R. Chen, S.X. Li, J.L. Wen, W.P. Jia, Finite element analysis about effects of stiffness distribution on stresses and elastic strain energy near the triple junction in a tricrystal, Mater. Sci. Eng. A. 282 (2000) 170–176. https://doi.org/10.1016/S0921-5093(99)00760-1.

[4] M. Li, D.J. Duquette, Y. Chen, Deformation Accommodation at Triple Junctions in Columnar-Grained Nickel, Metall. Mater. Trans. A Phys. Metall. Mater. Sci. 50 (2019) 52–57. https://doi.org/10.1007/s11661-018-4998-0.

[5] S.X. Li, D.B. Ren, W.P. Jia, C.R. Chen, X.W. Li, Z.G. Wang, On the stress distribution around a triple junction, Philos. Mag. A Phys. Condens. Matter, Struct. Defects Mech. Prop. 80 (2000) 1729–1741. https://doi.org/10.1080/01418610008219080.

[6] N. Pai, A. Prakash, I. Samajdar, A. Patra, Study of grain boundary orientation gradients through combined experiments and strain gradient crystal plasticity modeling, Int. J. Plast. 156 (2022) 103360. https://doi.org/10.1016/j.ijplas.2022.103360.

[7] S. Kobayashi, S. Tsurekawa, T. Watanabe, Grain boundary hardening and triple junction hardening in polycrystalline molybdenum, Acta Mater. 53 (2005) 1051–1057. https://doi.org/10.1016/j.actamat.2004.11.002.

[8] T. Eliash, M. Kazakevich, V.N. Semenov, E. Rabkin, Nanohardness of molybdenum in the vicinity of grain boundaries and triple junctions, Acta Mater. 56 (2008) 5640–5652. https://doi.org/10.1016/j.actamat.2008.07.036.

[9] M.S. Wu, J. Niu, A theoretical investigation into the nucleation of stable crack precursors in polycrystalline ice, Int. J. Fract. 68 (1993) 151–181. https://doi.org/10.1007/BF00032465.

[10] S. Kobayashi, T. Inomata, H. Kobayashi, S. Tsurekawa, T. Watanabe, Effects of grain boundary- and triple junction-character on intergranular fatigue crack nucleation in polycrystalline aluminum, J. Mater. Sci. 43 (2008) 3792–3799. https://doi.org/10.1007/s10853-007-2236-z.

[11] M.A. Charpagne, J.M. Hestroffer, A.T. Polonsky, M.P. Echlin, D. Texier, V. Valle, I.J. Beyerlein, T.M. Pollock, J.C. Stinville, Slip localization in Inconel 718: A three-dimensional and statistical perspective, Acta Mater. 215 (2021) 117037. https://doi.org/10.1016/j.actamat.2021.117037.

[12] N.L. Phung, V. Favier, N. Ranc, F. Valès, H. Mughrabi, Very high cycle fatigue of copper: Evolution, morphology and locations of surface slip markings, Int. J. Fatigue. 63 (2014) 68–77. https://doi.org/10.1016/j.ijfatigue.2014.01.007.

[13] Z.G. Wang, Z.F. Zhang, X.W. Li, W.P. Jia, S.X. Li, Orientation dependence of the cyclic deformation behavior and the role of grain boundaries in fatigue damage in copper crystals, Mater. Sci. Eng. A. 319–321 (2001) 63–73. https://doi.org/10.1016/S0921-5093(01)01055-3.

[14] J.F. Nye, Some geometrical relations in dislocated crystals, Acta Metall. 1 (1953) 153–162.

[15] E. Kröner, Continuum theory of dislocations and self-stresses, Springer, Berlin, 1958.

[16] K.Z. Troost, P. Van Der Sluis, D.J. Gravesteijn, Microscale elastic-strain determination by backscatter Kikuchi diffraction in the scanning electron microscope, Appl. Phys. Lett. 62 (1993) 1110–1112. https://doi.org/10.1063/1.108758.

[17] A.J. Wilkinson, G. Meaden, D.J. Dingley, High-resolution elastic strain measurement from electron backscatter diffraction patterns: New levels of sensitivity, Ultramicroscopy. 106 (2006) 307–313. https://doi.org/10.1016/j.ultramic.2005.10.001.

[18] W. Pantleon, Resolving the geometrically necessary dislocation content by conventional electron backscattering diffraction, Scr. Mater. 58 (2008) 994–997. https://doi.org/10.1016/j.scriptamat.2008.01.050.

[19] A.J. Wilkinson, D. Randman, Determination of elastic strain fields and geometrically necessary dislocation distributions near nanoindents using electron back scatter diffraction, Philos. Mag. 90 (2010) 1159–1177. https://doi.org/10.1080/14786430903304145.

[20] J. Jiang, T.B. Britton, A.J. Wilkinson, Evolution of dislocation density distributions in copper during tensile deformation, Acta Mater. 61 (2013) 7227–7239. https://doi.org/10.1016/j.actamat.2013.08.027.

[21] T.J. Ruggles, D.T. Fullwood, Estimations of bulk geometrically necessary dislocation density using high resolution EBSD, Ultramicroscopy. 133 (2013) 8–15. https://doi.org/10.1016/j.ultramic.2013.04.011.

[22] S. Das, F. Hofmann, E. Tarleton, Consistent determination of geometrically necessary dislocation density from simulations and experiments, Int. J. Plast. 109 (2018) 18–42. https://doi.org/10.1016/j.ijplas.2018.05.001.

[23] Y. Guo, D.M. Collins, E. Tarleton, F. Hofmann, A.J. Wilkinson, T. Ben Britton, Dislocation density distribution at slip band-grain boundary intersections, Acta Mater. 182 (2020) 172–183. https://doi.org/10.1016/j.actamat.2019.10.031.

[24] P.A. Shade, B. Blank, J.C. Schuren, T.J. Turner, P. Kenesei, K. Goetze, R.M. Suter, J. V. Bernier, S.F. Li, J. Lind, U. Lienert, J. Almer, A rotational and axial motion system load frame insert for in situ high energy x-ray studies, Rev. Sci. Instrum. 86 (2015) 093902. https://doi.org/10.1063/1.4927855.

[25] M. Kutsal, P. Bernard, G. Berruyer, P.K. Cook, R. Hino, A.C. Jakobsen, W. Ludwig, J. Ormstrup, T. Roth, H. Simons, K. Smets, J.X. Sierra, J. Wade, P. Wattecamps, C. Yildirim, H.F. Poulsen, C. Detlefs, The ESRF dark-field x-ray microscope at ID06, IOP Conf. Ser. Mater. Sci. Eng. 580 (2019). https://doi.org/10.1088/1757-899X/580/1/012007.

[26] S. Gustafson, W. Ludwig, P. Shade, D. Naragani, D. Pagan, P. Cook, C. Yildirim, C. Detlefs, M.D. Sangid, Quantifying microscale drivers for fatigue failure via coupled synchrotron X-ray characterization and simulations, Nat. Commun. 11 (2020) 3189. https://doi.org/10.1038/s41467-020-16894-2.

[27] H. Poulsen, Three-Dimensional X-Ray Diffraction Microscopy, Springer Berlin Heidelberg, Berlin, Heidelberg, 2004. https://doi.org/10.1007/b97884.

[28] J. V. Bernier, N.R. Barton, U. Lienert, M.P. Miller, Far-field high-energy diffraction microscopy: a tool for intergranular orientation and strain analysis, J. Strain Anal. Eng. Des. 46 (2011) 527–547. https://doi.org/10.1177/0309324711405761.

[29] R.M. Suter, D. Hennessy, C. Xiao, U. Lienert, Forward modeling method for microstructure reconstruction using x-ray diffraction microscopy: Single-crystal verification, Rev. Sci. Instrum. 77 (2006) 1–12. https://doi.org/10.1063/1.2400017.

[30] W. Ludwig, P. Reischig, A. King, M. Herbig, E.M. Lauridsen, G. Johnson, T.J. Marrow, J.Y. Buffire, Three-dimensional grain mapping by x-ray diffraction contrast tomography and the use of Friedel pairs in diffraction data analysis, Rev. Sci. Instrum. 80 (2009). https://doi.org/10.1063/1.3100200.

[31] M.A. Groeber, M.A. Jackson, DREAM.3D: A Digital Representation Environment for the Analysis of Microstructure in 3D, Integr. Mater. Manuf. Innov. 3 (2014) 56–72. https://doi.org/10.1186/2193-9772-3-5.

[32] J. Ahrens, B. Geveci, C. Law, C. Hansen, C. Johnson, Paraview: An end-user tool for large-data visualization, Vis. Handb. 717 (2005) 50031–50038.

[33] L. Renversade, R. Quey, W. Ludwig, D. Menasche, S. Maddali, R.M. Suter, A. Borbély, Comparison between diffraction contrast tomography and high-energy diffraction microscopy on a slightly deformed aluminium alloy, IUCrJ. 3 (2016) 32–42. https://doi.org/10.1107/S2052252515019995.

[34] W.A. Tayon, K.E. Nygren, R.E. Crooks, D.C. Pagan, In-situ study of planar slip in a commercial aluminum-lithium alloy using high energy X-ray diffraction microscopy, Acta Mater. 173 (2019) 231–241. https://doi.org/10.1016/j.actamat.2019.04.030.

[35] H. Simons, A. King, W. Ludwig, C. Detlefs, W. Pantleon, S. Schmidt, F. Stöhr, I. Snigireva, A. Snigirev, H.F. Poulsen, Dark-field X-ray microscopy for multiscale structural characterization, Nat. Commun. 6 (2015) 6098. https://doi.org/10.1038/ncomms7098.

[36] H.F. Poulsen, Current Opinion in Solid State & Materials Science Multi scale hard x-ray microscopy, Curr. Opin. Solid State Mater. Sci. 24 (2020) 100820. https://doi.org/10.1016/j.cossms.2020.100820.

[37] C. Yildirim, N. Mavrikakis, P.K. Cook, R. Rodriguez-Lamas, M. Kutsal, H.F. Poulsen, C.

Detlefs, 4D microstructural evolution in a heavily deformed ferritic alloy: A new perspective in recrystallisation studies, Scr. Mater. 214 (2022) 114689. https://doi.org/10.1016/j.scriptamat.2022.114689.

[38] C. Yildirim, C. Jessop, J. Ahlström, C. Detlefs, Y. Zhang, 3D mapping of orientation variation and local residual stress within individual grains of pearlitic steel using synchrotron dark field X-ray microscopy, Scr. Mater. 197 (2021) 113783. https://doi.org/10.1016/j.scriptamat.2021.113783.

[39] H.F. Poulsen, A.C. Jakobsen, H. Simons, S.R. Ahl, P.K. Cook, C. Detlefs, X-ray diffraction microscopy based on refractive optics, J. Appl. Crystallogr. 50 (2017) 1441–1456. https://doi.org/10.1107/S1600576717011037.

[40] H. Simons, A.C. Jakobsen, S.R. Ahl, H.F. Poulsen, W. Pantleon, Y.H. Chu, C. Detlefs, N. Valanoor, Nondestructive Mapping of Long-Range Dislocation Strain Fields in an Epitaxial Complex Metal Oxide, Nano Lett. 19 (2019) 1445–1450. https://doi.org/10.1021/acs.nanolett.8b03839.

[41] S.R. Ahl, Elements of a Method for Multiscale Characterization of Recrystallization in Deformed Metals, (2018).

[42] B.S. El-Dasher, B.L. Adams, A.D. Rollett, Viewpoint: Experimental recovery of geometrically necessary dislocation density in polycrystals, Scr. Mater. 48 (2003) 141–145. https://doi.org/10.1016/S1359-6462(02)00340-8.

[43] M. Kamaya, Assessment of local deformation using EBSD: Quantification of accuracy of measurement and definition of local gradient, Ultramicroscopy. 111 (2011) 1189–1199. https://doi.org/10.1016/j.ultramic.2011.02.004.

[44] J.D. Livingston, B. Chalmers, Multiple slip in bicrystal deformation, Acta Metall. 5 (1957) 322–327. https://doi.org/10.1016/0001-6160(57)90044-5.

[45] J.P. Hirth, The influence of grain boundaries on mechanical properties, Metall. Trans. 3 (1972) 3047–3067. https://doi.org/10.1007/BF02661312.

[46] M. Calcagnotto, D. Ponge, E. Demir, D. Raabe, Orientation gradients and geometrically necessary dislocations in ultrafine grained dual-phase steels studied by 2D and 3D EBSD, Mater. Sci. Eng. A. 527 (2010) 2738–2746. https://doi.org/10.1016/j.msea.2010.01.004.

[47] M. Kamaya, Measurement of local plastic strain distribution of stainless steel by electron backscatter diffraction, Mater. Charact. 60 (2009) 125–132. https://doi.org/10.1016/j.matchar.2008.07.010.

[48] A.J. Wilkinson, E.E. Clarke, T.B. Britton, P. Littlewood, P.S. Karamched, High-resolution electron backscatter diffraction: An emerging tool for studying local deformation, J. Strain Anal. Eng. Des. 45 (2010) 365–376. https://doi.org/10.1243/03093247JSA587.

[49] B.L. Adams, J. Kacher, EBSD-based microscopy: Resolution of dislocation density, Comput. Mater. Contin. 14 (2009) 183–194.

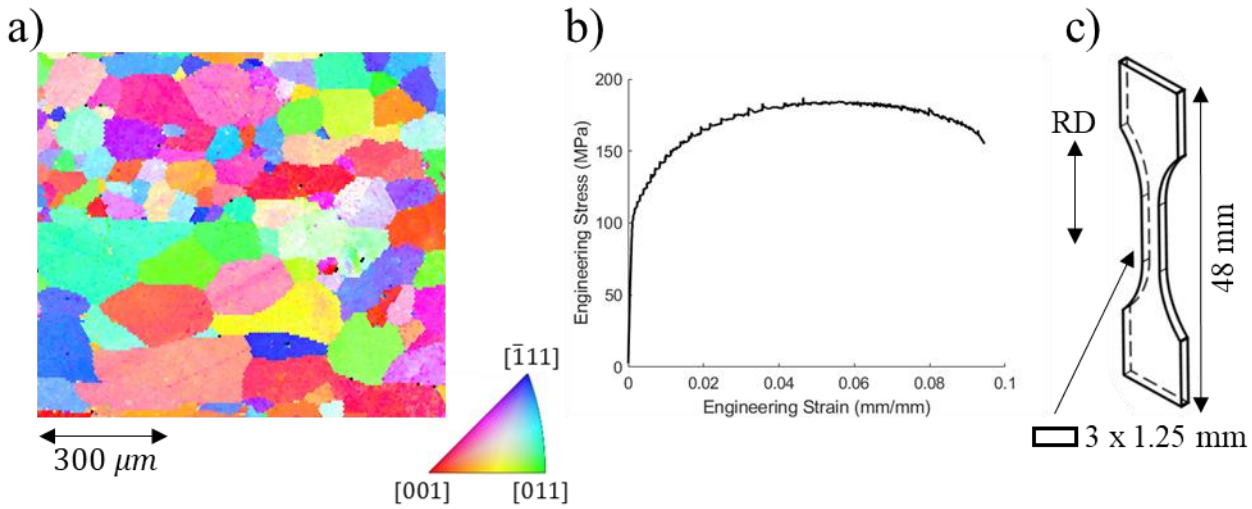

Figure 1: a) EBSD orientation map showing the microstructure of the sample after the chosen heat treatment, b) macroscopic engineering stress vs engineering strain for a c) dog bone style sample with the rolling direction (RD) indicated.

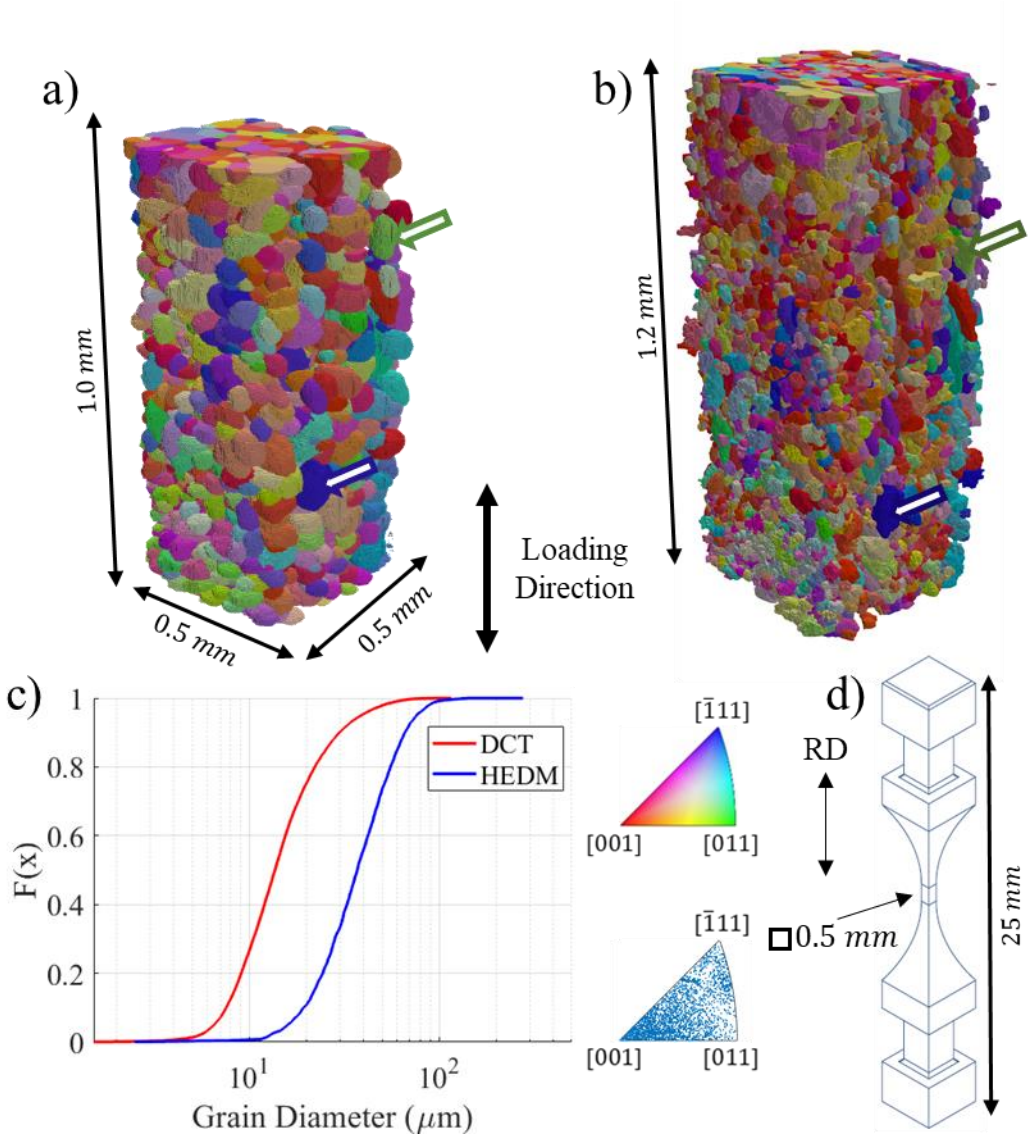

Figure 2: a) HEDM reconstruction, b) DCT reconstruction, c) cumulative distribution function of grain diameters for both HEDM and DCT, d) final specimen design with the rolling direction indicated. The green and blue arrows help track individual grains between the two reconstructions.

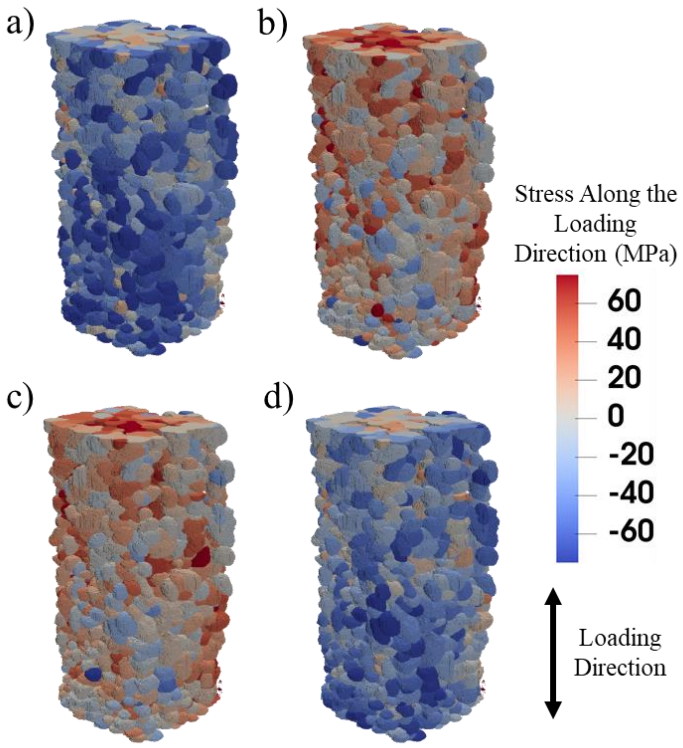

Figure 3: NF-HEDM reconstruction with grain morphologies colored with their corresponding stress along the loading direction from FF-HEDM for a) Unloaded – Prior to loading, b) Peak load (65 MPa) – First cycle, c) Peak load (55 MPa) – 100th cycle, d) Unloaded – After loading.

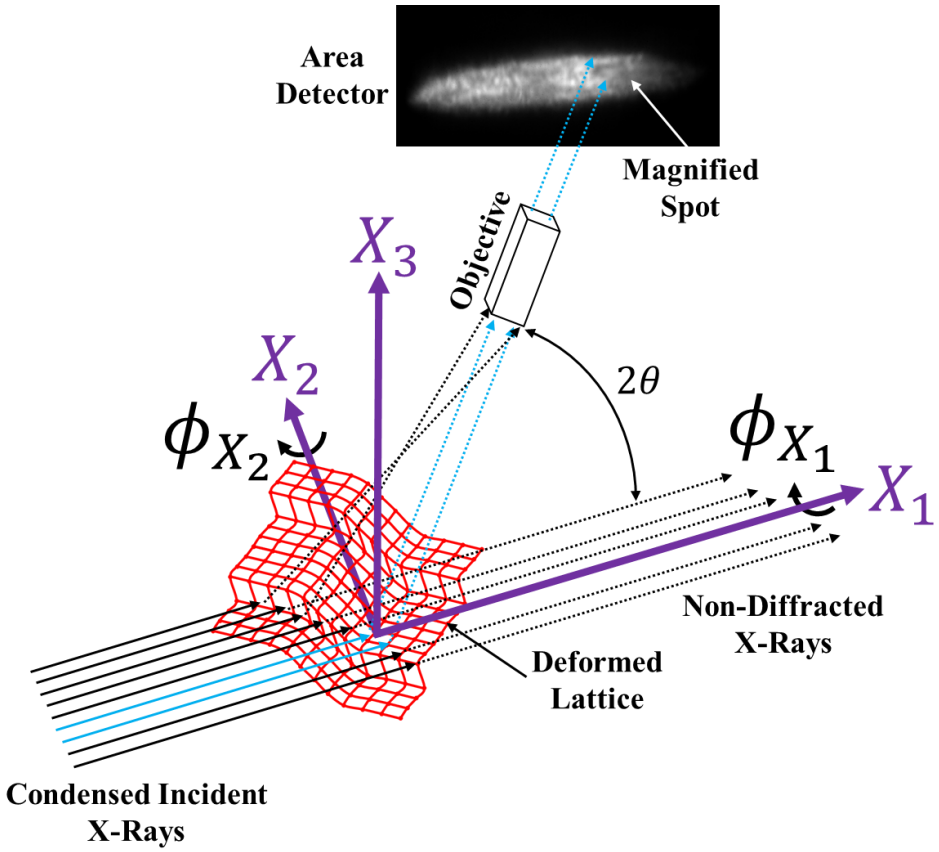

Figure 4: Experimental DFXM schematic.

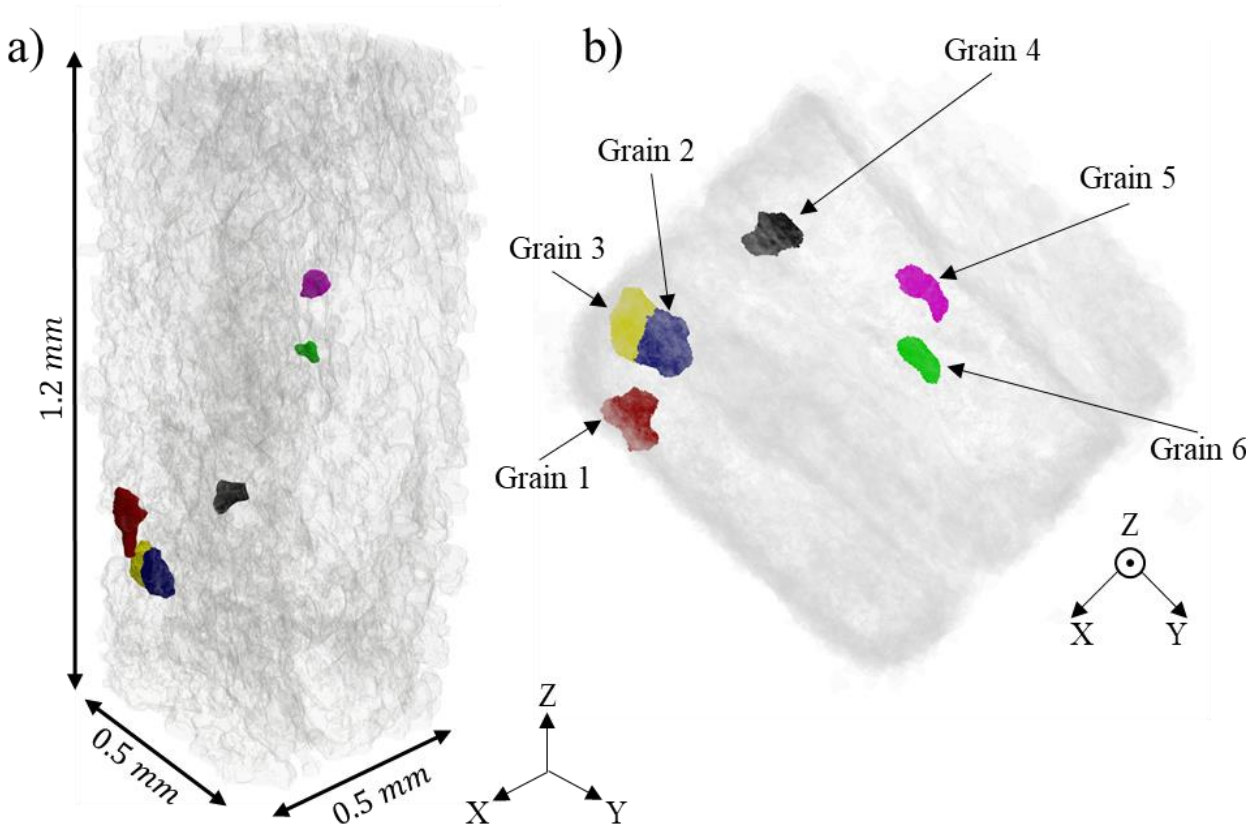

Figure 5: Relative locations of each grain within the DCT reconstruction from: a) the same perspective as shown in Figure 2, b) a top-down perspective. Colors of individual grains are arbitrary to provide sufficient contrast for viewing.

		Volume (x10^{-5} mm^3)			Non-local Curvature		IGM (°)		3DKAM (°)	
Grain	Equivalent Diameter DCT (μm^3)	DCT	DFXM	Difference $\frac{DCT - DFXM}{DFXM}$	Percent Positive	Percent Negative	Mean	Standard Deviation	Mean	Standard Deviation
1	58.49	10.5	9.41	11%	82.0%	18.0%	0.114	0.0655	0.0290	0.0138
2	57.42	9.91	9.22	7%	67.5%	32.5%	0.0660	0.0370	0.0157	0.0078
3	56.32	9.36	10.8	-14%	73.6%	26.4%	0.1350	0.0824	0.0221	0.0117
4	45.44	4.91	5.60	-12%	79.7%	20.3%	0.0244	0.0150	0.0067	0.0032
5	39.31	3.18	3.85	-17%	87.1%	12.9%	0.0233	0.0146	0.0071	0.0028
6	30.38	1.47	2.56	-43%	87.6%	12.4%	0.0139	0.0078	0.0050	0.0021

Table 1: Grain statistics from DCT and DFXM.

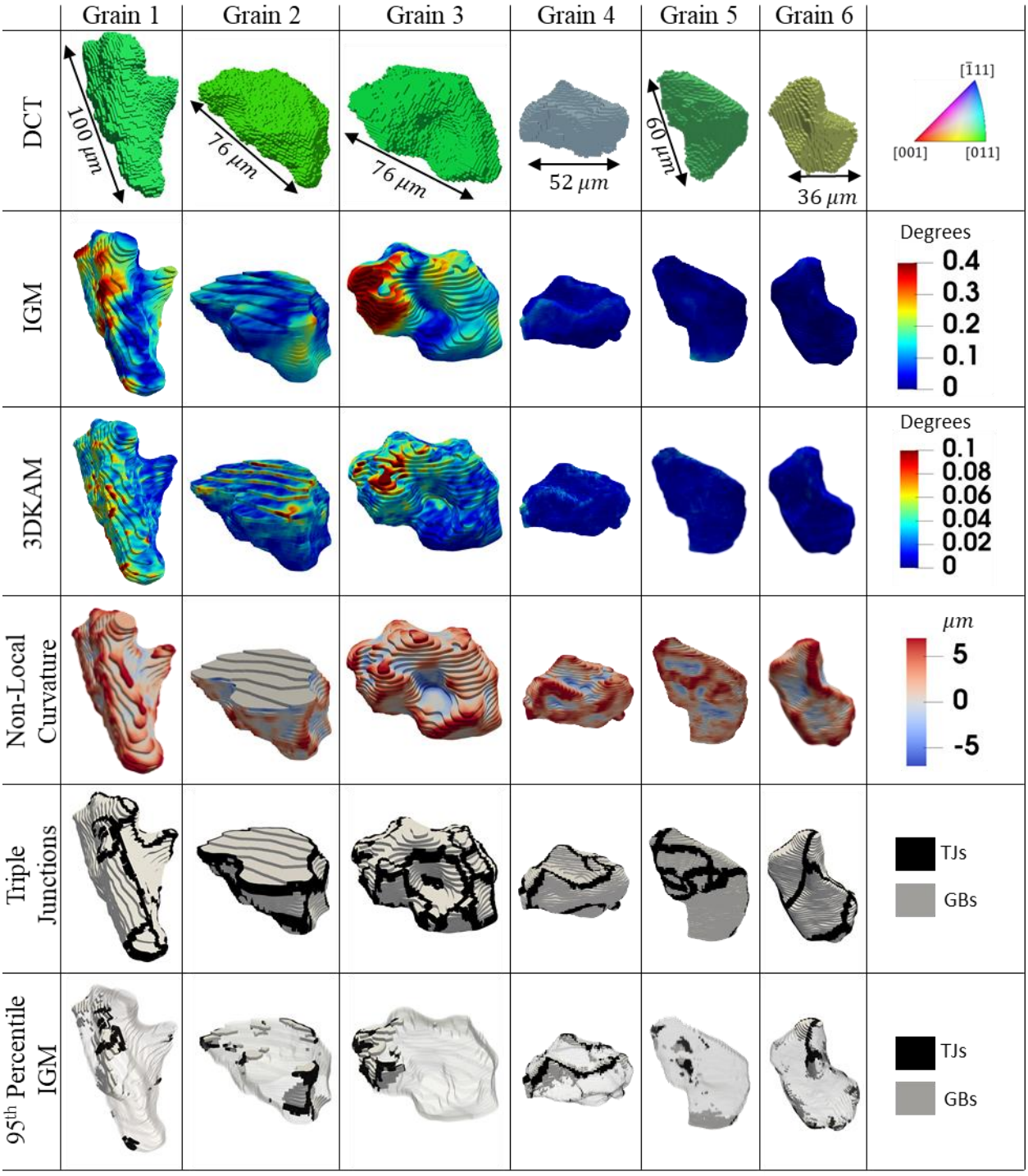

Figure 6: Comparison of extracted metrics (rows) for each grain (columns). Extracted metrics are: DCT reconstruction based on the inverse pole figure representation, intragranular misorientation (IGM), 3D kernal average misorientation (3DKAM), non-local curvature, triple junctions (TJs) vs grain boundaries (GBs) depictions, and voxels within the 95th percentile of the IGM (opaque voxels).

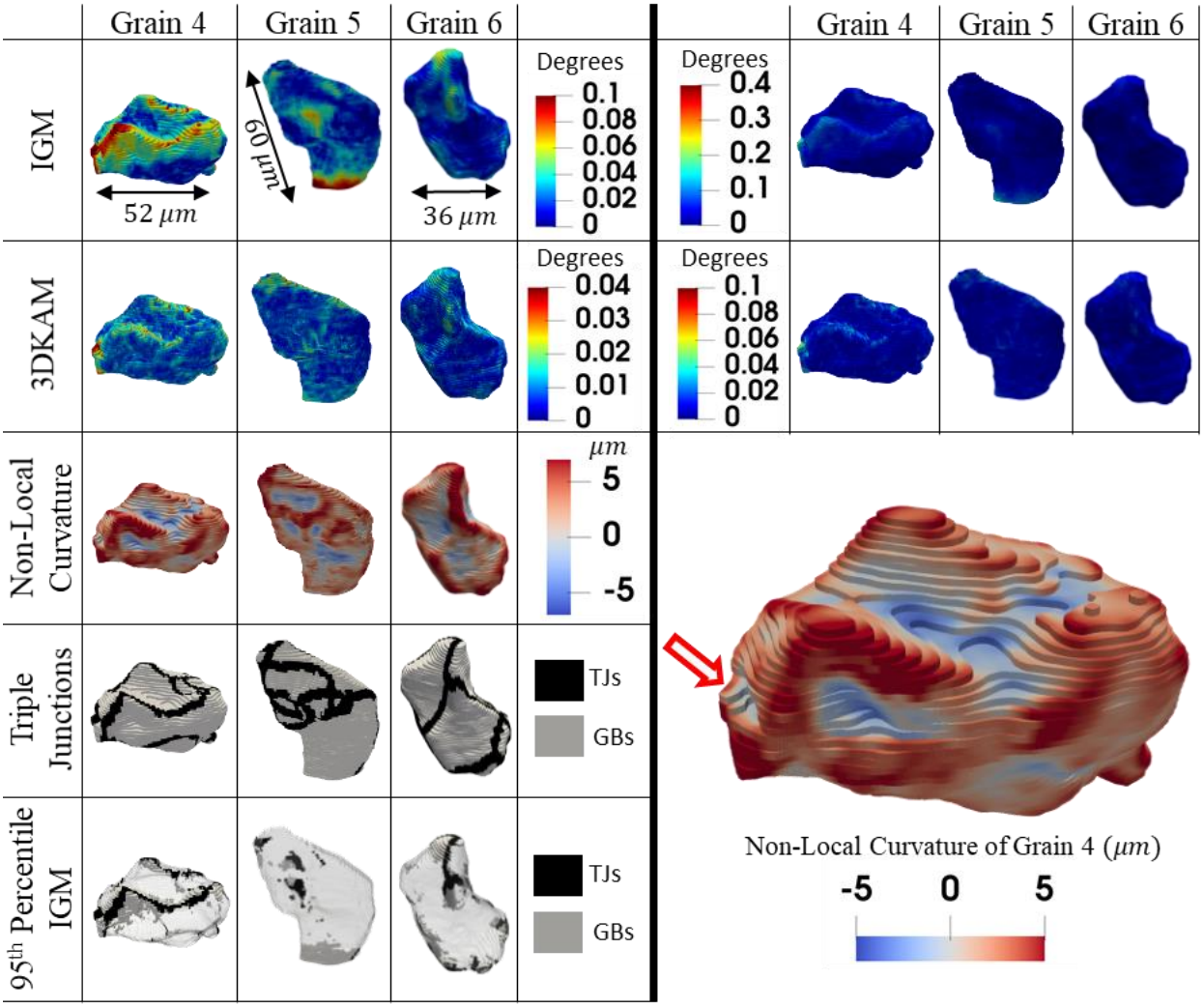

Figure 7: Comparison of extracted metrics (rows) for the lower deformation grains (columns) with relevant color scaling along with original scaling for comparison. Extracted metrics are: IGM, 3DKAM, non-local curvature, triple junctions (TJs) vs grain boundaries (GBs), and voxels within the 95th percentile of IGM (opaque voxels). Lower right corner shows an enlargement of grain 4's non-local curvature with a red reference arrow.

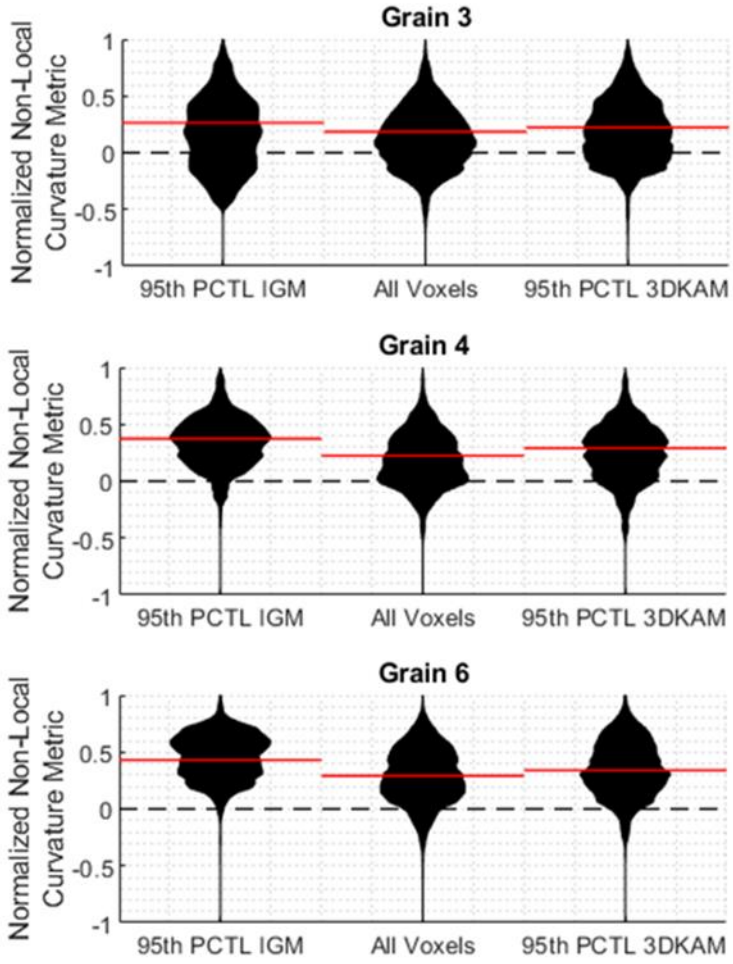

Figure 8: Violin plots comparing the non-local curvature values of all surface voxels of a single grain to the surface voxels included within the 95th percentile of both a) IGM and b) 3DKAM. The dashed line provides the zero line to aid in the determination of positive vs negative curvature while the red lines are the weighted sums of each distribution (where the normalized surface area acts as the weights). Only surface voxels, where curvature is estimated, are used in distributions and weighted sums.

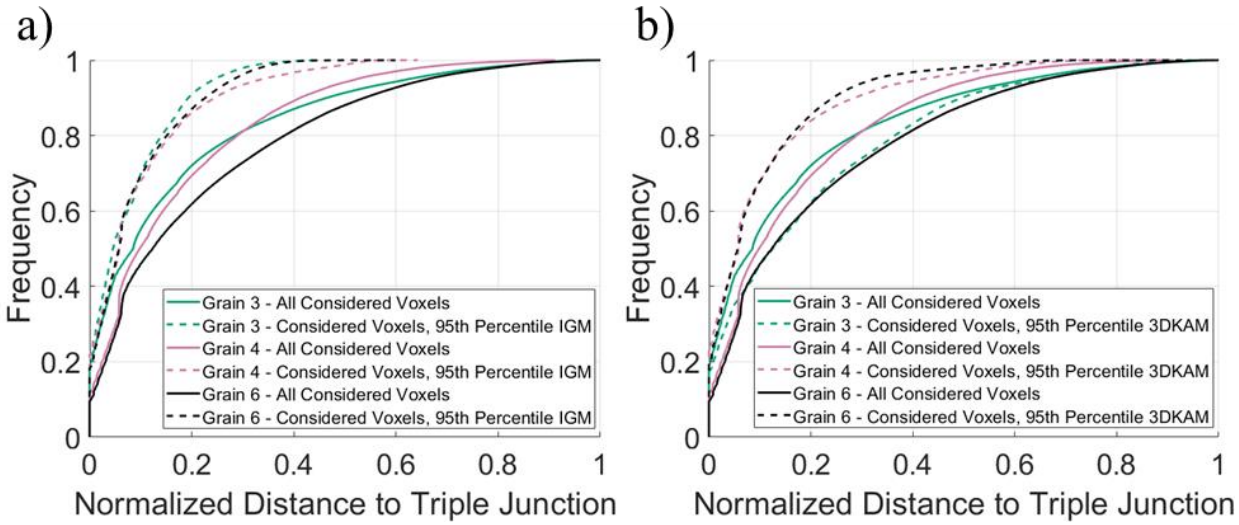

Figure 9: Cumulative distribution functions of the normalized distance to triple junctions of all considered voxels compared to the voxels within the 95th percentile of a) IGM and b) 3DKAM. Only voxels within 1 μm of the grain boundary are considered.

	All Considered Voxels		Considered Voxels in the 95th Percentile IGM			Considered Voxels in the 95th Percentile 3DKAM		
Grain	Mean (μm)	Standard Deviation (μm)	Mean (μm)	Standard Deviation (μm)	If a voxel is in the 95th percentile, is it statistically closer to a triple junction than an arbitrary voxel?	Mean (μm)	Standard Deviation (μm)	If a voxel is in the 95th percentile, is it statistically closer to a triple junction than an arbitrary voxel?
3	3.28	4.14	1.55	1.69	Yes [$t(2957935) = 189.6$, $p < 0.01$]	3.99	4.30	No [$t(3111265) = -95.6$, $p < 0.01$]
4	2.82	2.97	1.61	1.95	Yes [$t(2888574) = 226.3$, $p < 0.01$]	1.77	2.39	Yes [$t(3061755) = 233.8$, $p < 0.01$]
6	3.15	3.28	1.29	1.39	Yes [$t(1561213) = 233.5$, $p < 0.01$]	1.43	1.79	Yes [$t(1614306) = 243.0$, $p < 0.01$]

Table 2: Statistical comparison of the distance to a triple junction of all considered voxels to the voxels within the 95th percentile of either IGM or 3DKAM. Only voxels within 1 μm of the grain boundary are considered.

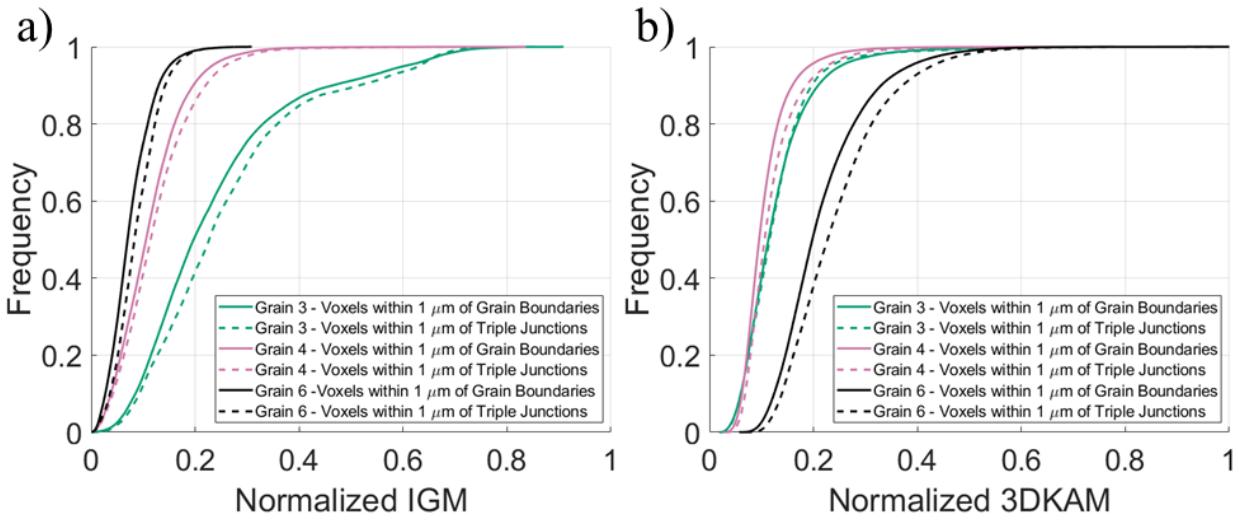

Figure 10: Cumulative distribution functions of the voxels within 1 μm of the grain boundaries compared to the voxels within 1 μm of the triple junctions for a) normalized IGM and b) normalized 3DKAM.

	IGM					3DKAM				
	Voxels within 1 μm of grain boundaries		Voxels within 1 μm of triple junctions		If a voxel is within 1 μm of a triple junction, is it statistically more likely to have higher value of IGM than a voxel which is only within 1 μm of a grain boundary?	Voxels within 1 μm of grain boundaries		Voxels within 1 μm of triple junctions		If a voxel is within 1 μm of a triple junction, is it statistically more likely to have a higher value of 3DKAM than a voxel which is is only within 1 μm of a grain boundary?
Grain	Mean (°)	Standard Deviation (°)	Mean (°)	Standard Deviation (°)		Mean (°)	Standard Deviation (°)	Mean (°)	Standard Deviation (°)	
3	0.1456	0.0951	0.1590	0.0965	Yes [t(3921585) = 127.2, p < 0.01]	0.0285	0.0156	0.0283	0.0152	No [t(3921585) = -11.8 , p < 0.01]
4	0.0316	0.0184	0.0347	0.0204	Yes [t(3513010) = 138.1, p < 0.01]	0.0099	0.0044	0.0112	0.0052	Yes [t(3513010) = 225.6, p < 0.01]
6	0.0175	0.0095	0.0202	0.0098	Yes [t(1906774) = 177.1, p < 0.01]	0.0066	0.0027	0.0074	0.0029	Yes [t(1906774) = 188.7, p < 0.01]

Table 3: Statistical comparison for both IGM and 3DKAM of voxels within 1 μm of grain boundaries to voxels within 1 μm of triple junctions.

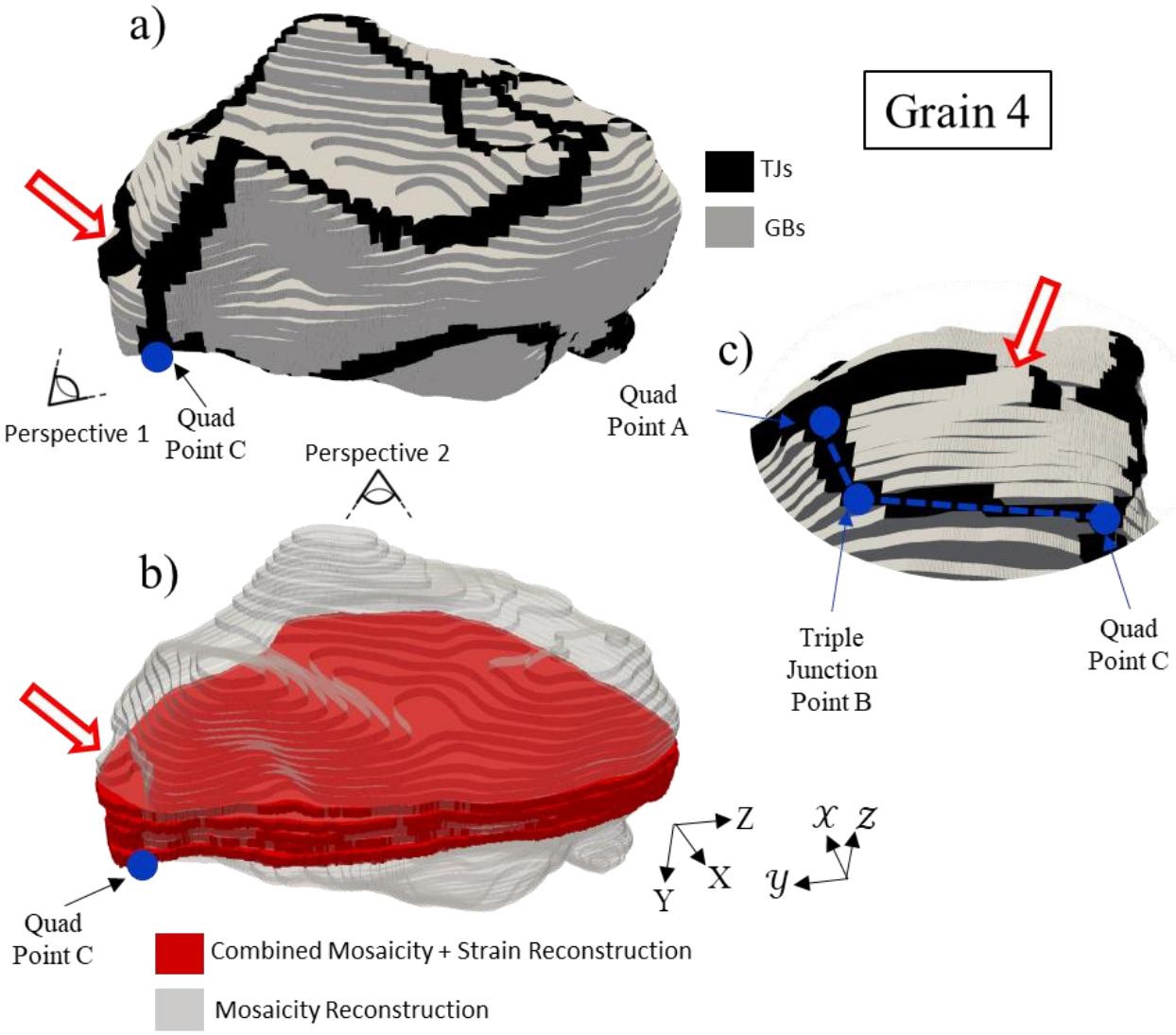

Figure 11: a) Triple junctions of grain 4 as shown in Figure 6. b) Relative location of combined mosaicity and strain reconstruction to the mosaicity reconstruction of grain 4. c) Zoom-in of a particular triple junction of grain 4 using Perspective 1 with lines AB and BC indicating the extracted voxels along the triple junction used in Figure 16. Perspective 2, normal to Z, is used in Figure 12-14. DCT coordinate system provided as X, Y, Z with loading direction along Z. DFXM coordinate system for grain 4 provided as $\mathcal{X}$, $\mathcal{Y}$, $\mathcal{Z}$ with loading direction approximately along $\mathcal{Y}$ and $[\mathcal{X}, \mathcal{Y}, \mathcal{Z}] = [X_1, X_2, X_3]$ during DFXM scanning of grain 4. Both coordinate systems correspond only to sub-figures a) and b).

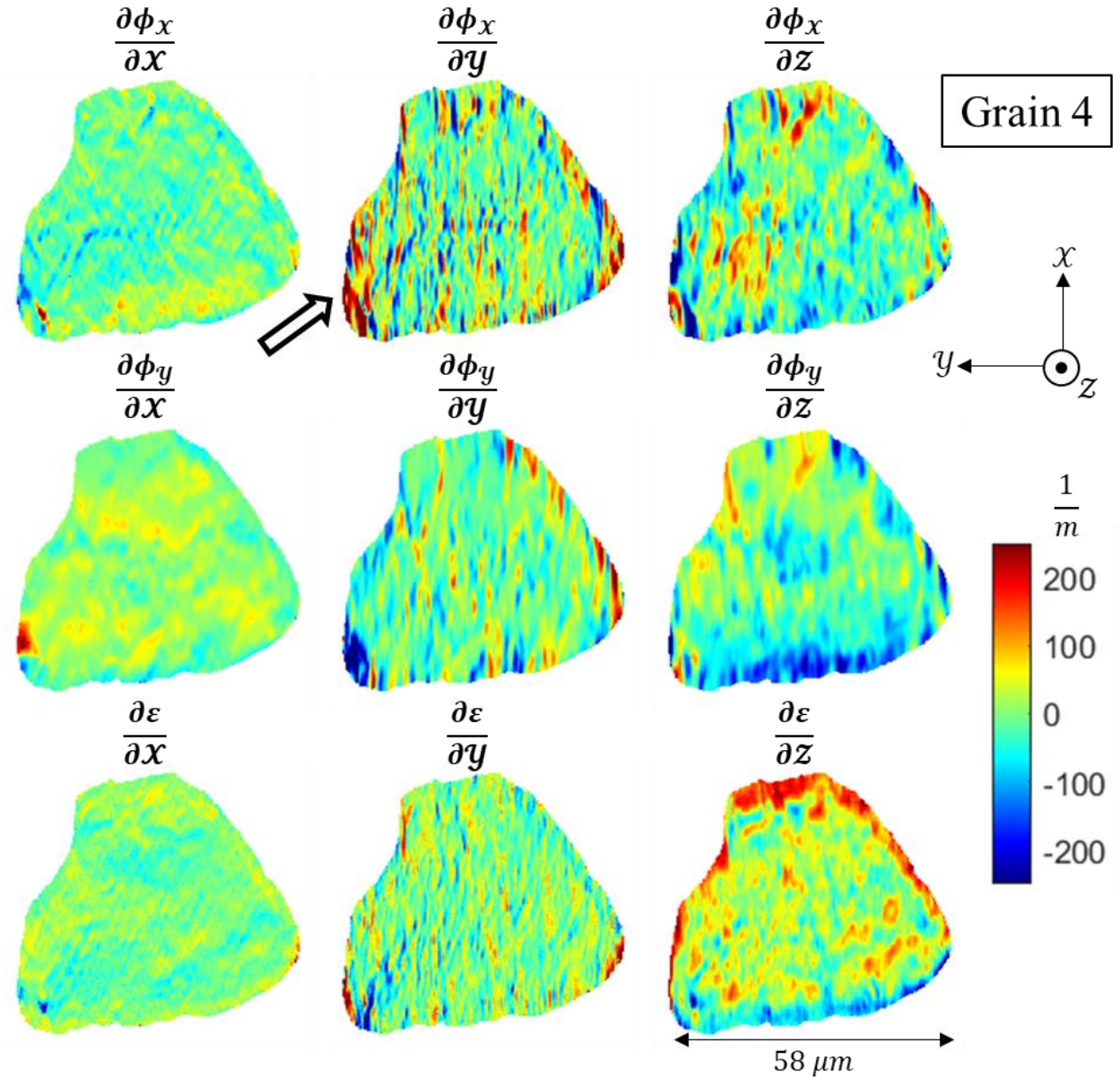

Figure 12: Plot of individual lattice rotation and elastic strain gradient components from a single slice of the combined mosaicity and strain reconstruction of grain 4 as viewed by Perspective 2 in Figure 11. The elastic strain, ε, is the component normal to grain 4's (111) plane of interest.

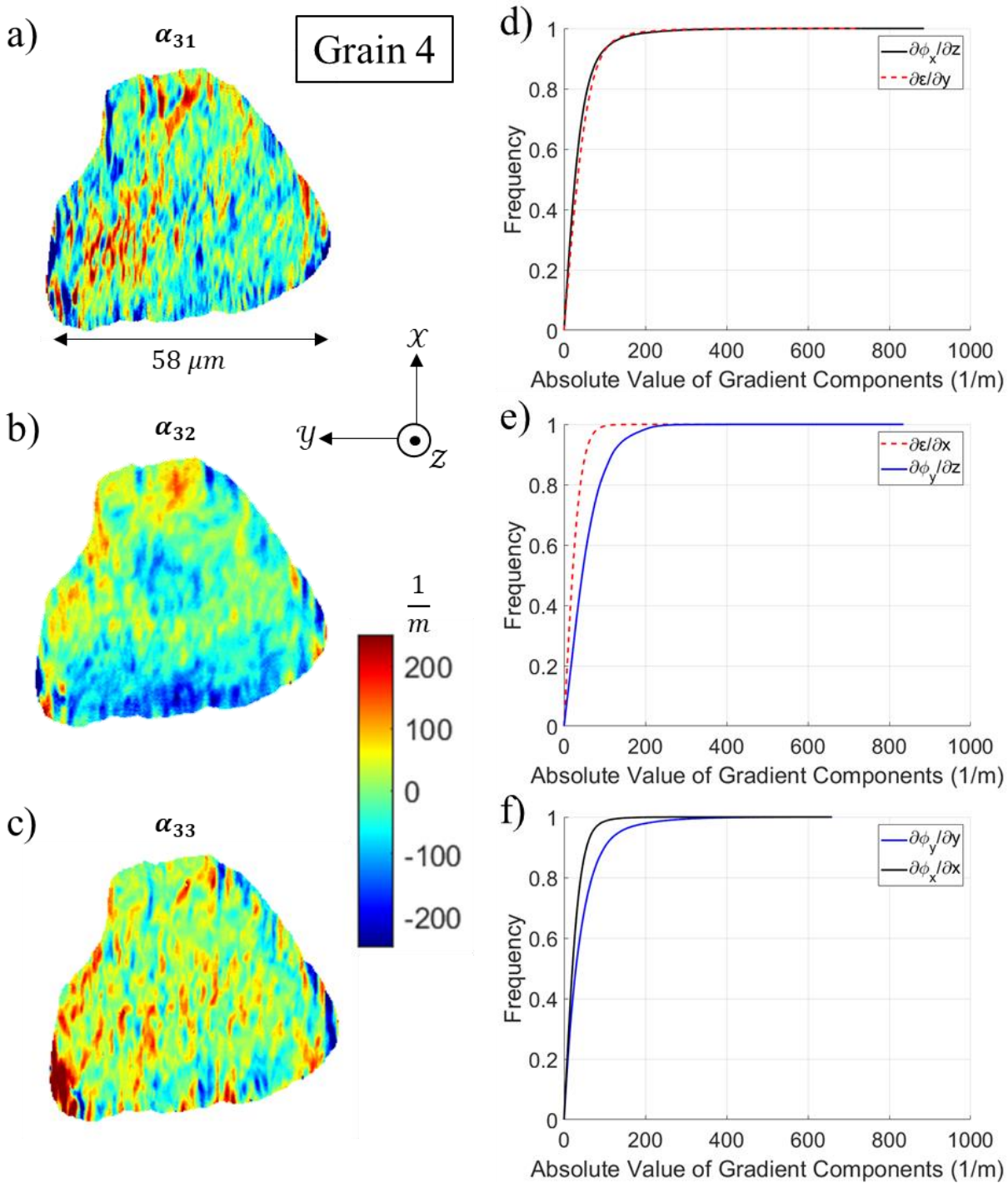

Figure 13: Nye tensor components, a) α_{31}, b) α_{32}, c) α_{33} from a single slice of the combined mosaicity and strain reconstruction of grain 4 as viewed by Perspective 2 in Figure 11. Cumulative distribution plots comparing the magnitude of each gradient component constructing the individual Nye tensor components d) α_{31}, e) α_{32}, f) α_{33}. The elastic strain, ε, is the component normal to grain 4's (111) plane of interest and its gradient is shown by dashed lines in d,e) while the lattice rotation gradients are shown in solid lines.

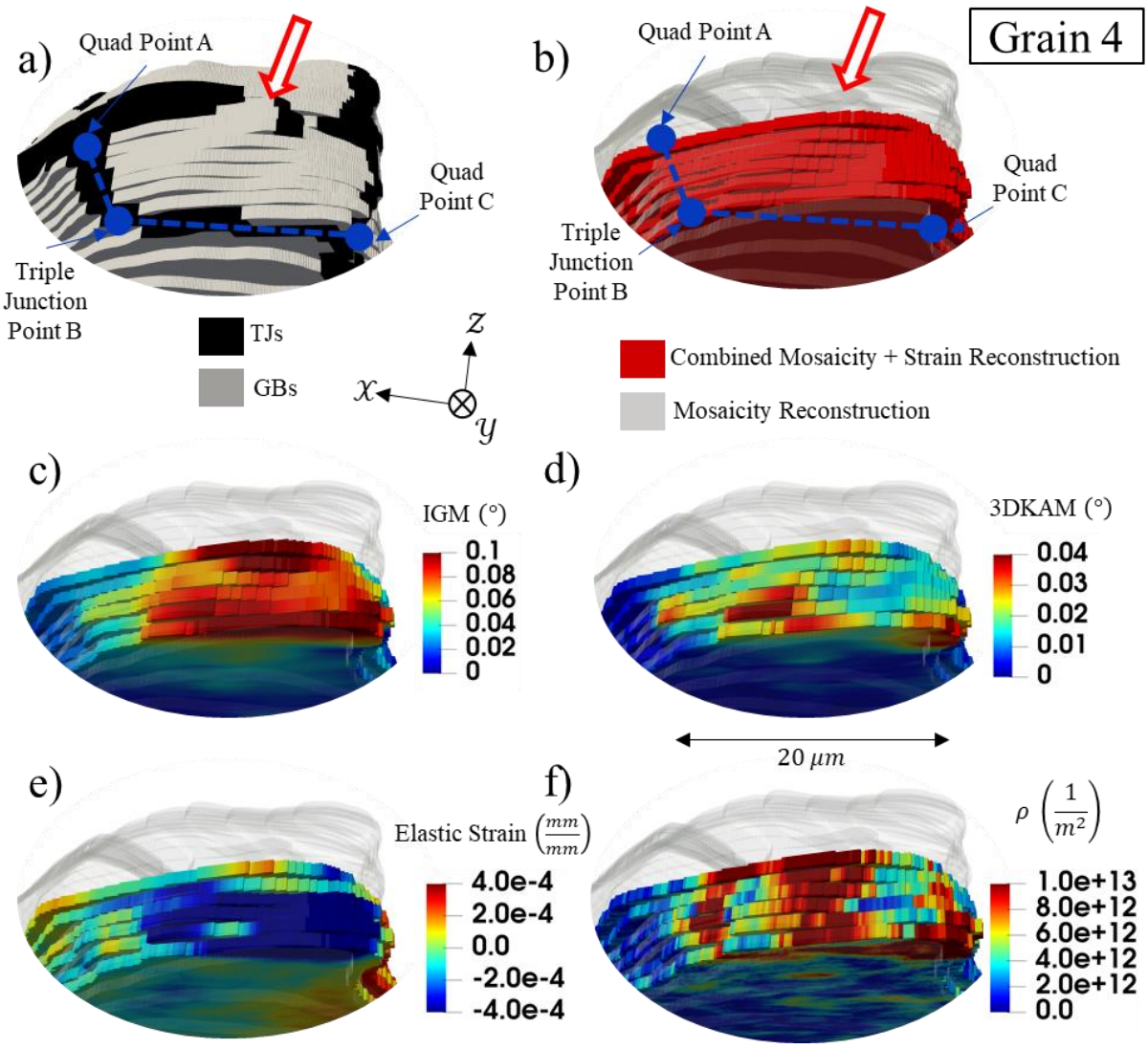

Figure 14: Zoom-in of grain 4 as seen through perspective 1. Relative location of the triple junction lines AB and BC with respect to: a) locations of grain 4's triple junctions, b) the combined mosaicity and strain reconstruction. Intragranular metrics from the combined mosaicity and strain reconstruction: c) IGM, d) 3DKAM, e) elastic strain normal to grain 4's (111) plane of interest, d) entrywise 1-norm estimate of the dislocation density.

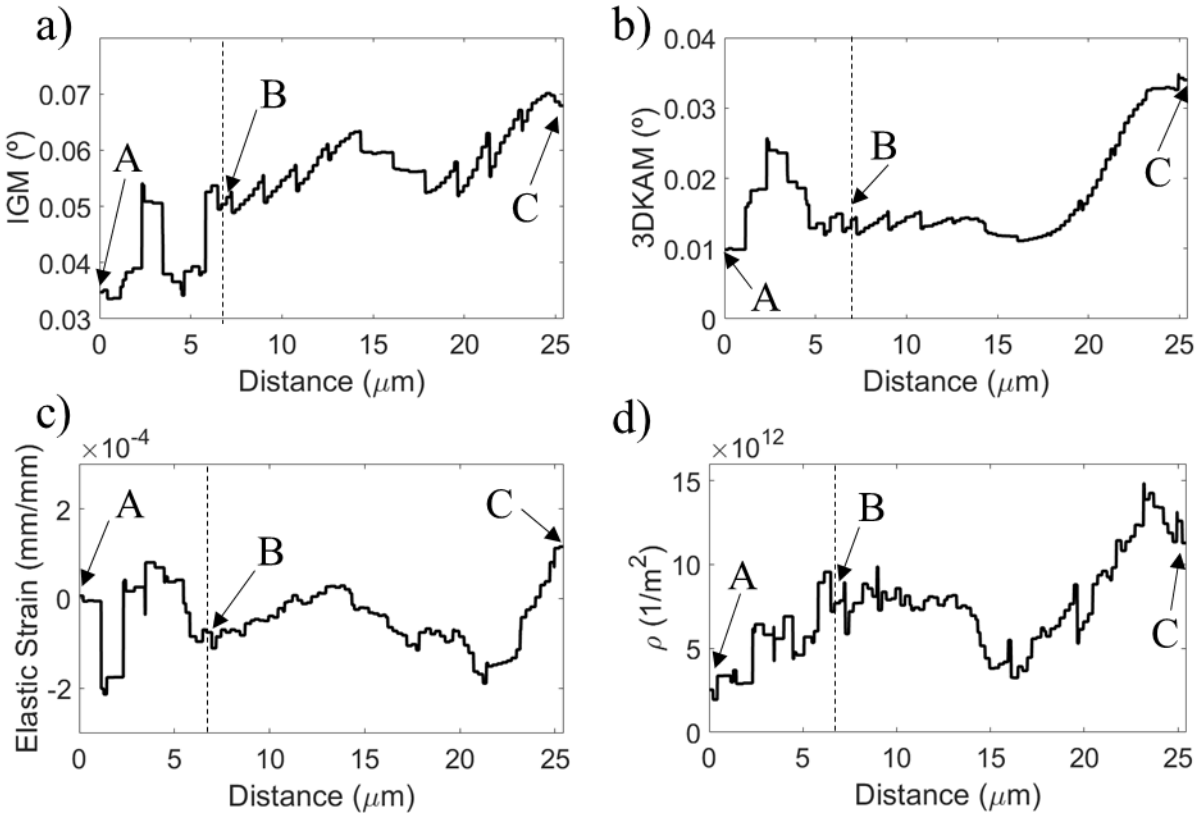

Figure 15: Line plots extracted from grain 4's combined mosaicity and strain reconstruction of a) IGM, b) 3DKAM, c) elastic strain normal to grain 4's (111) plane of interest, and d) entrywise one-norm estimate of the dislocation density, ρ. Positions A, B, and C in b) correspond to the line shown along a triple junction in Figure 11c and Figure 14a,b.

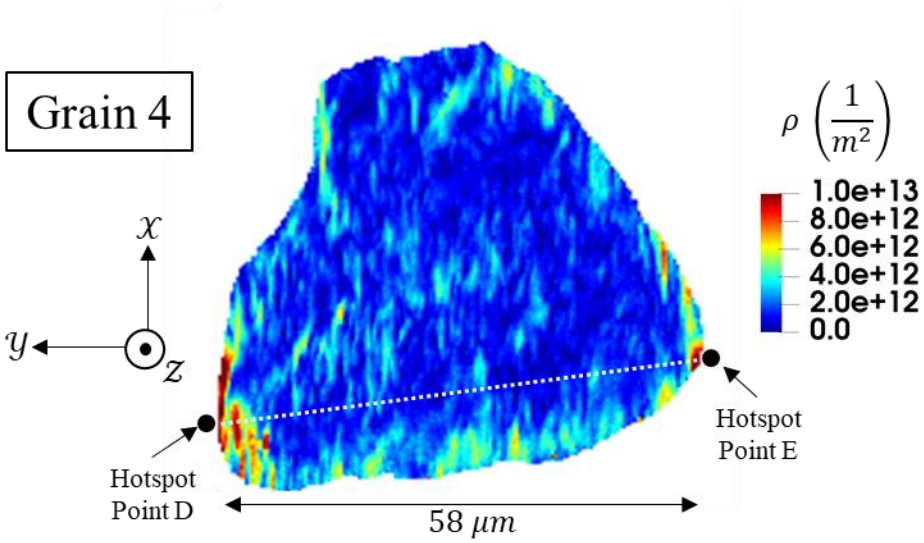

Figure 16: Entrywise one-norm estimate of the dislocation density from a single slice of the combined mosaicity and strain reconstruction of grain 4 as viewed by Perspective 2 in Figure 11.

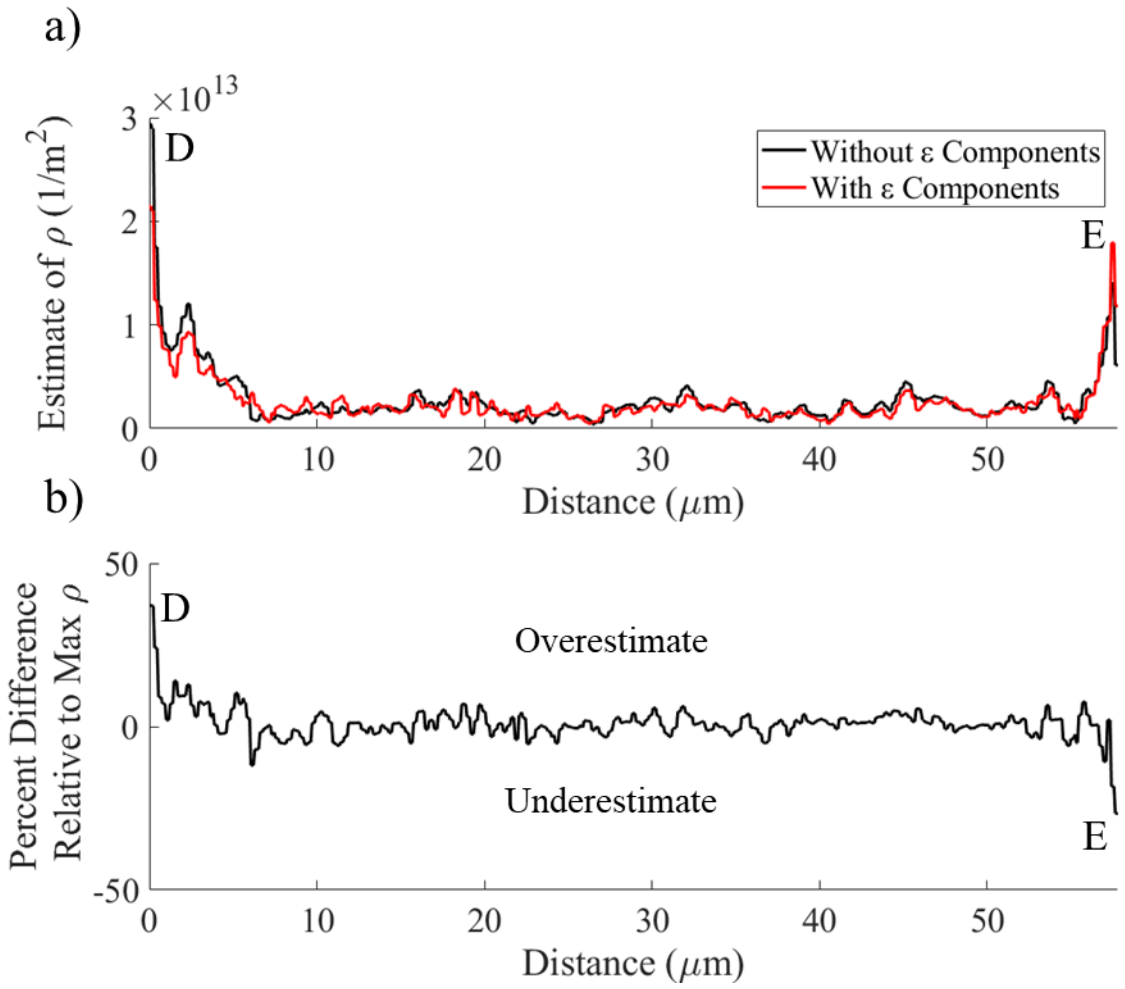

Figure 17: Line plots of data from the line between points D and E as seen in Figure 16. a) comparison between entrywise 1-norm estimates of ρ with and without contributions from elastic strain gradient components. b) percent difference of the entrywise 1-norm estimates of ρ in a) relative to the maximum ρ observed.

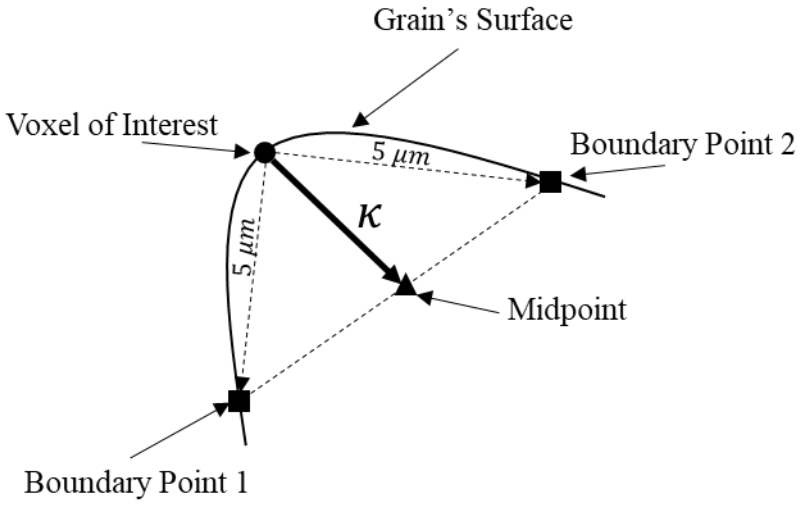

Figure A1: Schematic visualizing the spatial locations of the individual points relevant during the calculation of non-local curvature.

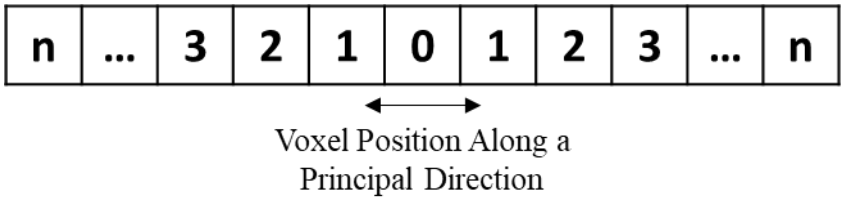

Figure C1: Schematic illustrating an increasing voxel position from a center voxel of interest along a single principal direction.

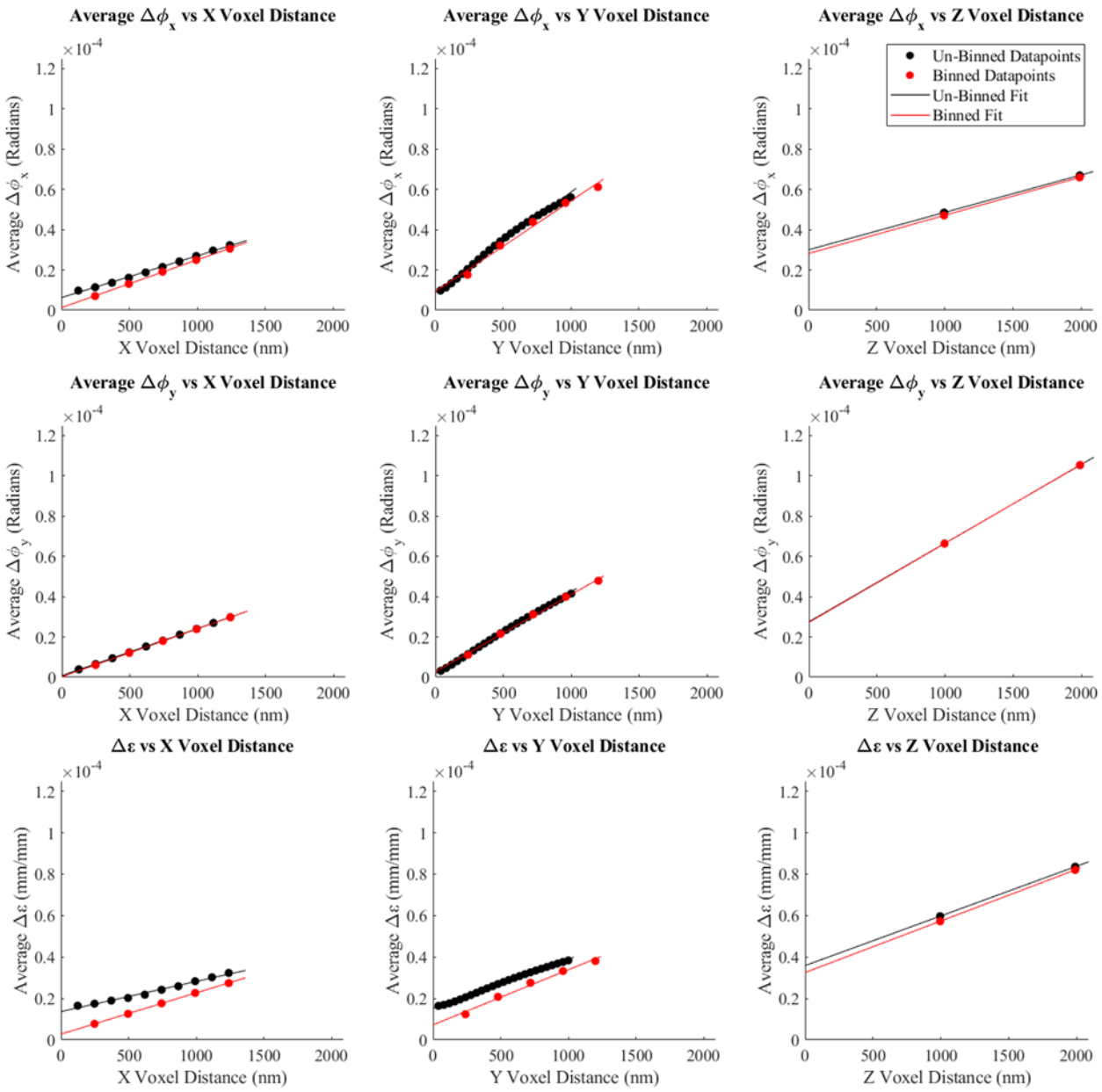

Figure C2: ΔM_i vs voxel distance of each angular and elastic strain component for each principal direction.

	$(\Delta M_i)_{BG_j}$ (-)		$\left(\frac{\partial M_i}{\partial X_j}\right)_{BG}$ $(1/m)$	
(M_i, X_j)	Un-Binned	Binned	Un-Binned	Binned
$(\phi_x, \mathcal{X})$	6.30E-06	1.31E-06	50.80	5.28
$(\phi_x, \mathcal{Y})$	8.92E-06	9.11E-06	223.12	37.97
$(\phi_x, \mathcal{Z})$	3.00E-05	2.81E-05	30.16	28.29
$(\phi_y, \mathcal{X})$	8.19E-07	2.49E-07	6.61	1.01
$(\phi_y, \mathcal{Y})$	1.91E-06	2.72E-06	47.66	11.33
$(\phi_y, \mathcal{Z})$	2.75E-05	2.72E-05	27.65	27.38
$(\varepsilon, \mathcal{X})$	1.37E-05	2.78E-06	110.21	11.23
$(\varepsilon, \mathcal{Y})$	1.52E-05	7.26E-06	378.99	30.23
$(\varepsilon, \mathcal{Z})$	3.59E-05	3.25E-05	36.04	32.68

Table C1: Tabulated values of the noise floors of ΔM_i for each angular/strain component and principal direction as well as the corresponding background noise of the corresponding spatial gradients.